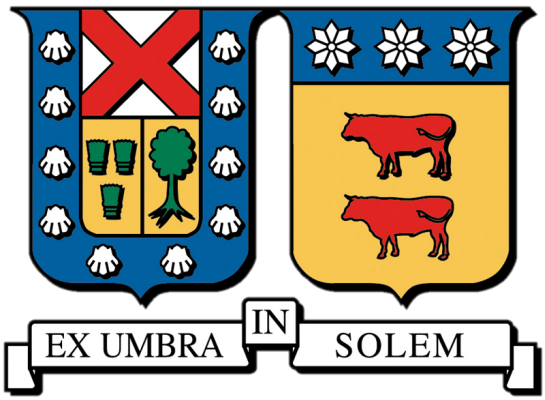
Cristóbal Benavides

PHYSICS BACHELOR'S THESIS



Universidad Técnica Federico Santa María

Campus San Joaquín, Santiago de Chile

Study of J/ψ Polarization in Pb-Pb Collisions at $\sqrt{S_{NN}} = 5.02$ TeV with the ATLAS Experiment

Supervisor: PhD. Nicolás Viaux M.

Co Supervisor: PhD. Sebastián Tapia A.

ACADEMIC COMMITTEE:

PhD. Diego Aristizábal S.

PhD. Sebastián Mendizabal C.

December, 2025

CONSTANCIA DE VALIDACIÓN Y CONFIDENCIALIDAD DE MONOGRAFÍA A REPOSITORIO ACADÉMICO

1.- IDENTIFICACIÓN DEL TRABAJO ACADÉMICO

Tipo de monografía (marcar una opción): ■ Memoria o trabajo de título ☐ Tesis de Postgrado

Título del trabajo: Study of J/ψ Polarization in Pb-Pb Collisions at $\sqrt{s_{NN}}$ = 5.02 TeV with the ATLAS Experiment

Nombre del candidato(a): Cristóbal Benavides

Carrera / Grado: Licenciatura en Física

Campus: San Joaquín **Departamento:** Departamento de Física

2.- VALIDACIÓN DEL PROFESOR GUÍA/DIRECTOR DE TESIS

Yo, Nicolás Viaux Maira, en mi calidad de guía del trabajo académico mencionado anteriormente **DEJO CONSTANCIA** que:

- He revisado esta versión del documento y corresponde a la versión final aprobada del trabajo.
- El trabajo cumple con los requisitos académicos y de formato establecidos por la institución.

3.- EVALUACIÓN DE CONFIDENCIALIDAD POR PROPIEDAD INDUSTRIAL (marcar una opción)

■ El trabajo **NO contiene** información que amerite confidencialidad y puede ser publicado de inmediato en repositorio con acceso abierto.

☐ El trabajo **CONTIENE** información con potenciales implicancias de propiedad industrial o intelectual y requiere un periodo de confidencialidad (**embargo**) por **(marcar una opción)**:

☐ 6 meses ☐ 12 meses ☐ 2 años ☐ 3 años ☐ 5 años ☐ 10 años

Fundamentación de la necesidad de confidencialidad (obligatorio si se solicita embargo):

4.- FIRMAS

Profesor(a) guía o director(a) de memoria o tesis:

Fecha: 16/01/2026 **Firma:** _____

Estudiante o Candidato(a):

Fecha: 16/01/2026 **Firma:** _____

ABSTRACT

The polarization of the J/ψ is studied with respect to the axis perpendicular to the event plane in the laboratory frame, using J/ψ mesons produced in Pb-Pb collisions at $\sqrt{s_{NN}}$ = 5.02 TeV. The analysis is based on data collected by the ATLAS detector during the 2023 and 2024 heavy-ion runs. The measurement is performed by analyzing the angular distribution of the J/ψ decay in the dimuon channel, in the rapidity region $|y| < 2.0$, for several transverse momentum intervals in the range 8< pT <24 GeV and for different centrality classes. The goal is to identify kinematic and centrality regions where a strong indication of polarization is present and to determine where sufficient statistical precision exists to further explore this effect. Measurements are reported in regions where hypothesis testing indicates the presence of polarization, showing a dependence on transverse momentum and centrality. Owing to the chosen reference frame, the observed polarization may be related to the properties and dynamics of the quark-gluon plasma formed in Pb-Pb collisions.

ACKNOWLEDGEMENTS

First and foremost, I would like to express my gratitude to my entire family; my parents, siblings, cousins, and grandparents. For their unwavering support throughout this entire period.

I am also deeply thankful to all my friends who helped me during this process, especially to Fabián, Jhohan$_s$, Clalo and Joe Metri for their encouragement and companionship.

I extend my sincere appreciation to my supervisor, Dr. Nicolás Viaux, for providing me with the opportunity to undertake this project. His understanding and patience were invaluable.

Finally, I would like to thank Dr. Luis Rosales for his crucial academic support and life advice, which guided me through many challenges.

Contents

Abstract **ii**

Acknowledgements **iii**

List of Figures **vi**

1 Particle Physiscs and Theoretical Framework **1**

1.1 Standard Model 1

1.2 Quantum chromodynamics 3

1.2.1 The QCD Lagrangian 4

1.2.2 Color 4

1.2.3 Asymptotic Freedom 5

1.2.4 Quarkonia 6

1.2.5 Quark Gluon Plasma in Heavy Ions Collisions 7

1.3 Discovery and Propierties of the J/ψ Meson 7

1.3.1 Parity 8

1.3.2 Charge conjugation 8

1.3.3 J/ψ Classification as a Polar Vector Meson 9

1.4 J/ψ Polarization 10

1.4.1 Helicity conservation 10

1.4.2 Angular Distribution 12

List of Tables **1**

2 LHC and ATLAS experiment **15**

2.1 Large Hadron Collider 15

2.2 ATLAS detector 16

2.3 Coordinate system of the Atlas detector 16

2.4 Inner s 17

2.5 Calorimeters 18

2.6 Muon Spectrometer 19

2.7 Muon Reconstruction 20

2.8 Muon Identification 22

3 Results **24**

3.1 Di Muon Invariant Mass Spectrum in Heavy Ions Collisions 24

3.2 λ_θ Measurement for J/ψ Polarization 25

3.2.1 J/ψ Candidates 26

3.2.2 Event Plane 26

3.2.3 Centrality 27

3.2.4 $0.1 - 20\%$ Centrality 28

3.2.5 20-40% Centrality 30

3.2.6 40-60% Centrality 33

3.2.7 60-85% Centrality 35

3.3 Backup 37

3.4 pT dependence of λ_θ 44

4 Concluding Remarks **46**

4.1 Summary 46

4.2 Future directions 46

References **48**

LIST OF FIGURES

1.1 Standard model picture of elementary particles 2
1.2 meassurments of α_s at different $|q|$ scales 6
1.3 Diagram of helicity conservation in the decay of a gauge boson into a fermion-antifermion pair. Red arrows indicate the spin orientations of the outgoing f and $\bar{f}$ and the black arrows represent the direction of the fermion flux. 11
1.4 Helicity conservation in the decay J/Ψ in to lepton and anti-lepton pair (left) and the effect on the total angular momentum of the di lepton system as seen in the J/Ψ rest frame (right). 11
1.5 Coordinate system for measurement of a two body decay distribution, axes and angles are defined in the rest frame of the decaying particle 12
1.6 Sketch for the decay $J/\psi \to l^+l^-$, with the notation used for axis and angles in the J/ψ rest frame 13

2.1 Schematics of CERN accelerator complex 15
2.2 Atlas detector layout illustration 16
2.3 ATLAS coordinate system at LHC 17
2.4 Computer generated image of the ATLAS inner detector 18
2.5 Ilustration of ATLAS calorimeter and different components of ECAL and HCAL 19

3.1 Dimuon invariant mass spectrum in O+O collisions at $\sqrt{S_{NN}} =$ 5.36 TeV recorded in 2025. The distribution is shown for muons passing p_T >2.75 GeV and $0 < |\eta| < 2.5$ and selected using the trigger HLT_mu3_L1MU3V. The histogram is scaled to unit integral. The distribution was built by combining each negatively charged muon with each positively charged muon in a given event, resulting in a combinatorial background. 24

3.2 Dimuon invariant mass spectrum in Ne+Ne collisions at $\sqrt{S_{NN}} =$ 5.36 TeV recorded in 2025. The distribution is shown for muons passing p_T >2.75 GeV and $0 < |\eta| < 2.5$ and selected using the trigger HLT_mu3_L1MU3V. The histogram is scaled to unit integral. The distribution was built by combining each negatively charged muon with each positively charged muon in a given event, resulting in a combinatorial background. 25
3.3 Schematic Diagram of reaction plane 27
3.4 Angular distribution of $J/\psi \rightarrow \mu^+\mu^-$ candidates as a function of cos(θ) in the centrality region 0.1-20% and in the transverse momentum range of $8 <$ pT < 10 GeV, with $\lambda_\theta = 0.43 \pm 0.01$ and a hypothesis test result of 20 σ 28
3.5 Angular distribution of $J/\psi \rightarrow \mu^+\mu^-$ candidates as a function of cos(θ) in the centrality region 0.1-20% and in the transverse momentum range of $10 <$ pT < 12 GeV, with $\lambda_\theta = 0.27 \pm 0.02$, and a hypothesis test result of 16.9 σ 29
3.6 Angular distribution of $J/\psi \rightarrow \mu^+\mu^-$ candidates as a function of cos(θ) in the centrality region 0.1-20% and in the transverse momentum range of $12 <$ pT < 14 GeV, with $\lambda_\theta = 0.21 \pm 0.02$, and a hypothesis test result of 8.5 σ 29
3.7 Angular distribution of $J/\psi \rightarrow \mu^+\mu^-$ candidates as a function of cos(θ) in the centrality region 0.1-20% and in the transverse momentum range of $14 <$ pT < 16 GeV, with $\lambda_\theta = 0.22 \pm 0.03$, and a hypothesis test result of 6.8 σ 30
3.8 Angular distribution of $J/\psi \rightarrow \mu^+\mu^-$ candidates as a function of cos(θ) in the centrality region 20-40% and in the transverse momentum range of $8 <$ pT < 10 GeV, with $\lambda_\theta = 0.54 \pm 0.02$, and a hypothesis test result of 29.7 σ 30
3.9 Angular distribution of $J/\psi \rightarrow \mu^+\mu^-$ candidates as a function of cos(θ) in the centrality region 20-40% and in the transverse momentum range of $10 <$ pT < 12 GeV, with $\lambda_\theta = 0.36 \pm 0.02$, and a hypothesis test result of 14.1 σ 31
3.10 Angular distribution of $J/\psi \rightarrow \mu^+\mu^-$ candidates as a function of cos(θ) in the centrality region 20-40% and in the transverse momentum range of $12 <$ pT < 14 GeV, with $\lambda_\theta = 0.24 \pm 0.03$, and a hypothesis test result of 5.8 σ 31

3.11 Angular distribution of $J/\psi \rightarrow \mu^+\mu^-$ candidates as a function of cos(θ) in the centrality region 20-40% and in the transverse momentum range of 14 < pT < 16 GeV, with $\lambda_\theta = 0.26 \pm 0.04$, and a hypothesis test result of 4.6 σ 32
3.12 Angular distribution of $J/\psi \rightarrow \mu^+\mu^-$ candidates as a function of cos(θ) in the centrality region 20-40% and in the transverse momentum range of 16 < pT < 18 GeV, with $\lambda_\theta = 0.26 \pm 0.06$, and a hypothesis test result of 1.3 σ 32
3.13 Angular distribution of $J/\psi \rightarrow \mu^+\mu^-$ candidates as a function of cos(θ) in the centrality region 40-60% and in the transverse momentum range of 8 < pT < 10 GeV, with $\lambda_\theta = 0.56 \pm 0.04$, and a hypothesis test result of 15.5 σ 33
3.14 Angular distribution of $J/\psi \rightarrow \mu^+\mu^-$ candidates as a function of cos(θ) in the centrality region 40-60% and in the transverse momentum range of 10 < pT < 12 GeV, with $\lambda_\theta = 0.39 \pm 0.04$, and a hypothesis test result of 7.8 σ 33
3.15 Angular distribution of $J/\psi \rightarrow \mu^+\mu^-$ candidates as a function of cos(θ) in the centrality region 40-60% and in the transverse momentum range of 12 < pT < 14 GeV, with $\lambda_\theta = 0.25 \pm 0.05$, and a hypothesis test result of 3.1 σ 34
3.16 Angular distribution of $J/\psi \rightarrow \mu^+\mu^-$ candidates as a function of cos(θ) in the centrality region 40-60% and in the transverse momentum range of 14 < pT < 16 GeV, with $\lambda_\theta = 0.23 \pm 0.07$, and a hypothesis test result of 0.4 σ 34
3.17 Angular distribution of $J/\psi \rightarrow \mu^+\mu^-$ candidates as a function of cos(θ) in the centrality region 60-85% and in the transverse momentum range of 8 < pT < 10 GeV, with $\lambda_\theta = 0.45 \pm 0.07$, and a hypothesis test result of 5.1 σ 35
3.18 Angular distribution of $J/\psi \rightarrow \mu^+\mu^-$ candidates as a function of cos(θ) in the centrality region 60-85% and in the transverse momentum range of 10 < pT < 12 GeV, with $\lambda_\theta = 0.25 \pm 0.08$, and a hypothesis test result of 0.5 σ 35
3.19 Angular distribution of $J/\psi \rightarrow \mu^+\mu^-$ candidates as a function of cos(θ) in the centrality region 60-85% and in the transverse momentum range of 12 < pT < 14 GeV, with $\lambda_\theta = 0.42 \pm 0.11$, and a hypothesis test result of 0.1 σ 36

3.20 Angular distribution of $J/\psi \rightarrow \mu^+\mu^-$ candidates as a function of cos(θ) in the centrality region 60-85% and in the transverse momentum range of 14 < pT < 16 GeV, with $\lambda_\theta = 0.52 \pm 0.16$, and a hypothesis test result of 0.8 σ 36
3.21 Angular distribution of $J/\psi \rightarrow \mu^+\mu^-$ candidates as a function of cos(θ) in the centrality region 0.1-20% and in the transverse momentum range of 16 < pT < 18 GeV, with $\lambda_\theta = 0.09 \pm 0.04$, and a hypothesis test result of 0.8 σ 37
3.22 Angular distribution of $J/\psi \rightarrow \mu^+\mu^-$ candidates as a function of cos(θ) in the centrality region 0.1-20% and in the transverse momentum range of 18 < pT < 20 GeV, with $\lambda_\theta = 0.19 \pm 0.05$, and a hypothesis test result of 1.8 σ 38
3.23 Angular distribution of $J/\psi \rightarrow \mu^+\mu^-$ candidates as a function of cos(θ) in the centrality region 0.1-20% and in the transverse momentum range of 20 < pT < 22 GeV, with $\lambda_\theta = 0.16 \pm 0.06$, and a hypothesis test result of 1.4 σ 38
3.24 Angular distribution of $J/\psi \rightarrow \mu^+\mu^-$ candidates as a function of cos(θ) in the centrality region 0.1-20% and in the transverse momentum range of 22 < pT < 24 GeV, with $\lambda_\theta = 0.22 \pm 0.08$, and a hypothesis test result of 1.2 σ 39
3.25 Angular distribution of $J/\psi \rightarrow \mu^+\mu^-$ candidates as a function of cos(θ) in the centrality region 20-40% and in the transverse momentum range of 18 < pT < 20 GeV, with $\lambda_\theta = 0.10 \pm 0.06$, and a hypothesis test result of -1.7 σ 39
3.26 Angular distribution of $J/\psi \rightarrow \mu^+\mu^-$ candidates as a function of cos(θ) in the centrality region 20-40% and in the transverse momentum range of 20 < pT < 22 GeV, with $\lambda_\theta = 0.23 \pm 0.09$, and a hypothesis test result of -0.4 σ 40
3.27 Angular distribution of $J/\psi \rightarrow \mu^+\mu^-$ candidates as a function of cos(θ) in the centrality region 20-40% and in the transverse momentum range of 22 < pT < 24 GeV, with $\lambda_\theta = 0.19 \pm 0.10$, and a hypothesis test result of -1.9 σ 40
3.28 Angular distribution of $J/\psi \rightarrow \mu^+\mu^-$ candidates as a function of cos(θ) in the centrality region 40-60% and in the transverse momentum range of 16 < pT < 18 GeV, with $\lambda_\theta = 0.32 \pm 0.10$, and a hypothesis test result of 0.4 σ 41

3.29 Angular distribution of $J/\psi \rightarrow \mu^+\mu^-$ candidates as a function of cos(θ) in the centrality region 40-60% and in the transverse momentum range of 18 < pT < 20 GeV, with $\lambda_\theta = 0.39 \pm 0.13$, and a hypothesis test result of -0.6 σ 41
3.30 Angular distribution of $J/\psi \rightarrow \mu^+\mu^-$ candidates as a function of cos(θ) in the centrality region 40-60% and in the transverse momentum range of 20 < pT < 22 GeV, with $\lambda_\theta = 0.06 \pm 0.13$, and a hypothesis test result of -0.1 σ 42
3.31 Angular distribution of $J/\psi \rightarrow \mu^+\mu^-$ candidates as a function of cos(θ) in the centrality region 40-60% and in the transverse momentum range of 22 < pT < 24 GeV, with $\lambda_\theta = 0.19 \pm 0.17$, and a hypothesis test result of -0.6 σ 42
3.32 Angular distribution of $J/\psi \rightarrow \mu^+\mu^-$ candidates as a function of cos(θ) in the centrality region 60-85% and in the transverse momentum range of 16 < pT < 18 GeV, with $\lambda_\theta = -0.06 \pm 0.15$, and a hypothesis test result of 0.8 σ 43
3.33 Angular distribution of $J/\psi \rightarrow \mu^+\mu^-$ candidates as a function of cos(θ) in the centrality region 60-85% and in the transverse momentum range of 18 < pT < 20 GeV, with $\lambda_\theta = 0.14 \pm 0.22$, and a hypothesis test result of -0.6 σ 43
3.34 Angular distribution of $J/\psi \rightarrow \mu^+\mu^-$ candidates as a function of cos(θ) in the centrality region 60-85% and in the transverse momentum range of 20 < pT < 22 GeV, with $\lambda_\theta = 0.02 \pm 0.25$, and a hypothesis test result of -1.6 σ 44
3.35 Angular distribution of $J/\psi \rightarrow \mu^+\mu^-$ candidates as a function of cos(θ) in the centrality region 60-85% and in the transverse momentum range of 22 < pT < 24 GeV, with $\lambda_\theta = 0.22 \pm 0.31$, and a hypothesis test result of -3.9 σ 44
3.36 pT dependence of λ_θ, horizontal bars show the size of the pT ranges, with the data points being located at the center of each range, with different values of λ_θ for each centrality range. 45

Chapter 1

Particle Physiscs and Theoretical Framework

1.1 Standard Model

In order to describe the most fundamental behavior of matter in our universe, the idea of considering building blocks had been developed, representing elementary particles that constitute all matter. These particles can be classified in to leptons and quarks, whose interaction are mediated by force-carryng bosons. this theoretical framework is known as standard model, wich clasifies elementary particles according to their fundamental properties.

Elemtary particles interact with each other by four fundamental forces, electromagnetism, weak force, strong force and gravity. The gravitacional force is negelcted in the disscusion of this particles interactions because of the extreamly small gravitacional forces between two individual particles. Knowing this, we can classify these particles in the following way:

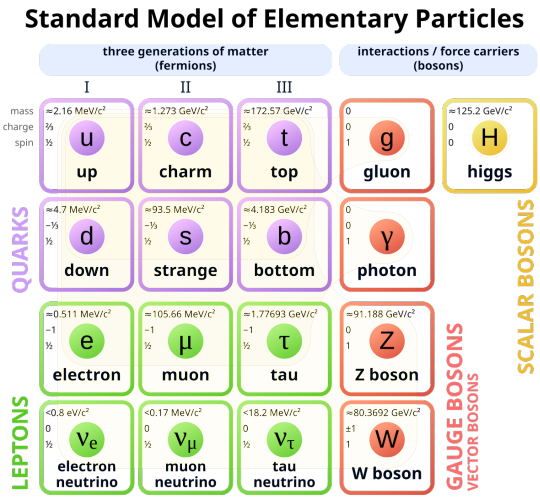


Figure 1.1: Standard model picture of elementary particles

Quarks: Protons and Nucleons are bound states of three quarks, wich are known as Baryons. There is another type of bound states formed by 2 quarks, known as mesons. These quarks can interact with electromagnetism, weak force and strong force. This is the only type of fundamental particles that have these characteristics. There are 6 types of quarks (and their antiparticles):

- Up (u), Down (d)
- Charm (c), Strange (s)
- Top (t), Bottom (b)

Leptons: This group of elementary particles is composed of charged and neutral particles. Charge particles interact with electromagnetic and weak force, neutral particles can only interact by weak force. these particles are:

- Electron (e^-), Muon (μ^-), Tau (τ^-)
- Electron neutrino (ν_e), Muon neutrino (ν_μ), Tau neutrino (ν_τ)

Force Carrying Particles: The three forces of relevance to particle physics are mediated by a Quantum Field Theory (QFT) corresponding to the exchange of a spin-1 force-carrying particle, known as a Gauge boson:

- Gluon: this is a masless particle that madiates strong interaction, being the QCD gauge boson that can only couples to quarks

- Photon: this is a masless boson as well as the gluon, but it madiates the electromagetic interaction, correspoding to the QED gauge boson.

- W^+, W^- and Z: the weak interaction among paricles is madiated by any of this bosons depending on the carge they carry. for negative and positive-weak interaction, the corresponding boson is the W^- and W^+ bosons respectivly, for neutral-weak interaction the interaction is mediated by the electrally neutral boson Z.

- Higgs boson: the final element of the standard model, discovered by the ATLAS and CMS experiments at the Large Hadron Collider (LHC) in 2012. it provides the mechanism by which all other particles acquire mass.

1.2 Quantum chromodynamics

In QFT all the forces in nature are the result of particle exchange, for example, the electromagnetic force among two electrons is mediated by a masless photon corresponding to the single U(1) local gauge symetry generator. QCD is mediated by eight masless gluons corresponfing to the eight generators of the SU(3) local gauge symmetry, then, the single charge of QED is repleced by three "colour" charges, r, b and g, where colour is a label for the orthogonal states in the SU(3) colour space. In QED the antiparticles have the oppposite electric charge of the quark, similary, in QCD the antiquarks carry the opposite colour charge of the quark.

1.2.1 The QCD Lagrangian

The QCD lagrangian reads:

$$\mathcal{L}_{\mathrm{QCD}}(x) = -\frac{1}{4}G_a^{\mu\nu}G^a_{\mu\nu} + i\sum_{j=1}^{n}\bar{\psi}_j^{\alpha}\gamma^{\mu}(D_{\mu})_{\alpha\beta}\psi_j^{\beta} - \sum_{j=1}^{n}m_j\bar{\psi}_j^{\alpha}\psi_{j,\alpha}, \tag{1.1}$$

where

$$G^a_{\mu\nu} = \partial_{\mu}A^a_{\nu} - \partial_{\nu}A^a_{\mu} + gf_{abc}A^b_{\mu}A^c_{\nu}, \quad a = (1, 2, .., 8), \tag{1.2}$$

these are the Yang-Mills field strengths constructed from the gluon fields A^a_{μ}, ψ_j is the field of the quark with j color.

$$(D_{\mu})_{\alpha\beta} \equiv \delta_{\alpha\beta}\partial_{\mu} - ig\sum_{a}\frac{1}{2}\lambda^a_{\alpha\beta}A^a_{\mu}, \tag{1.3}$$

is the covariant derivate, which is applicated in the coulor component $\alpha, \beta =$ red, blue and yellow, $\lambda^a_{\alpha\beta}$ are the eight colour matrices $(3x3)$ and f_{abc} are real structure constants, this terms close the $SU(3)$ Lie algebra:

$$[T_a, T_b] = if_{abc}T_c \tag{1.4}$$

1.2.2 Color

Quantum Electrodynamics (QED) interaction is mediated by a single masless photon corresponding to the U(1) local gauge symmetry and QCD is mediated by eight masless gluons corresponding to the eight generators of the SU(3) local gauge symmetry. now the single charge of QED is replaced by three conserved colour charges, r, b and g, here we refer to colour as a label for the ortogonal states of the SU(3) colour space, then quarks who carry colour charge lives in this colour states.

QCD is invariant under unitary transformations in colour space so the strength of QCD interaction is independient of the colour charge of the quark.

Antiquarks carry the opossite colour charge to the quarks, $\overline{r}, \overline{g}, \overline{b}$.

The three colour states are represented by the colour wave-functions:

$$r = \begin{pmatrix} 1 \\ 0 \\ 0 \end{pmatrix}, \quad g = \begin{pmatrix} 0 \\ 1 \\ 0 \end{pmatrix} \quad \text{and} \quad b = \begin{pmatrix} 0 \\ 0 \\ 1 \end{pmatrix}. \tag{1.5}$$

1.2.3 Asymptotic Freedom

The variation of the strength of the QCD coupling (α_s) with energy scale is one of the most defining characteristics of QCD. At high energy (or short distance) regime, (α_s) $\sim$ 0.1 GeV, this happens at $|q| > 100$ Gev, wich is the typical scale for modern high energy collider experiments. If we look for low energy (or large distance) regime where $|q| \sim$ 1GeV , it results that $\alpha_s \sim \mathcal{O}(1)$. Evidently this phenomena makes impossible to study QCD as a pertubative theory at low energy scales (where systems exhibit hadronization), but this is not the case for the high energy scenario where Quarks and Gluons behave almost like free particles where α_s is sufficiently small to use perturbation theory again. This property of QCD is known as asymptotic freedom.

The running QCD coupling constant is expressed as:

$$\alpha_s(|q^2|) = \frac{12\pi}{(11n - 2f)\ln(|q^2|/\Lambda^2)}, \tag{1.6}$$

where n is the number of colour (3, in the standard model), f is the number of flavours (6, in the standard model) and Λ is the characteristic energy scale of QCD, then α_s shows an inverse logarithmic dependence on the transferred momentum in the interaction, as shown in fig 1.2.

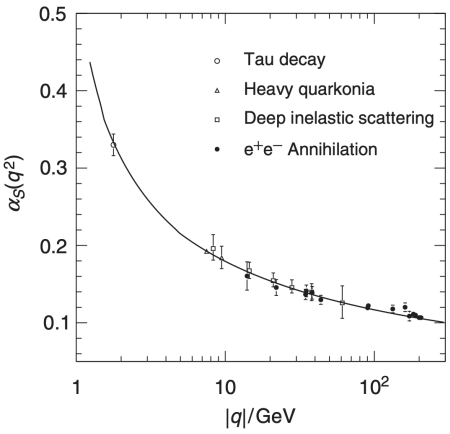


Figure 1.2: meassurments of α_s at different $|q|$ scales

1.2.4 Quarkonia

The quark family Up(u), down(d) and strange(s) is denominated as light quarks, while charm(c), bottom(b) and top(t) are called heavy quarks. Bound satates conformed by these heavy quarks with their corresponding anti-particles are called quarkonia. This mesons are flavorless, neutrally charged, their own anti-particle and short-lived due to matter-antimatter annihilation.

Light quarks in a meson move at relativistic speeds, as the mass of the bound state is much larger than the mass of the individual quarks. However due to the mass of heavy quarks the relative velocity in the boundstates is small enough to warrant a Non Relativistic QCD approach.

An early, but still effective technique to study the masses spectrum of quarkonium is the use of effective potentials and using the fact that the motion of the quarks that comprise the quarkonium state is non-relativistic we can assume that they move in a static potential, one of the most popular potential models is the Cornell potential [1]:

$$V(r) = \frac{a}{r} + br, \tag{1.7}$$

where r is the effective radius of the quarkonium state, a and b are parameters.

The first part of the potential ($\frac{a}{r}$) correspond to the potential induced by one gluon ex-change between the quark and its anti-quark, this term is known as the coulumbic part of the potential because of how the interaction is goberned by this parameter in short distances.

The second term (br) is known as the confinement part of the potential as the the potential becomes stronger while incresing the distance of the quark-antiquark system due to the lineal dependence of r.

1.2.5 Quark Gluon Plasma in Heavy Ions Collisions

Nuclear physics has traditionally focused on studying matter at densities comparable to those found within the atomic nucleus. This regime is characterized by a specific energy density, approximately $\epsilon \sim$0.15 GeV/fm^3.

High-energy nuclear physics extends this study to significantly higher energy densities, often several orders of magnitude greater. This subfield involves investigating matter composed of strongly interacting particles, such as the proton and neutron, and generating new forms of matter at extreme energy densities through high-energy collisions of nuclei with nuclei, and other experimental probes.

At these extreme densities, the matter can no longer be simply described in terms of composite particles (hadrons). Instead, it is described in terms of its fundamental constituents: quarks and gluons. This state is generally referred to as the Quark-Gluon Plasma (QGP).

1.3 Discovery and Propierties of the J/ψ Meson

A narrow resonance at 3.1 Gev in the e^+e^- invariant mass spectrum was observed in 1974 in collisions of 28 GeV protons at the Brookhaven Alternating Gradient Synchrotron (AGS) and in electron- positron collisions at Stanford Linear Accelerator Centre (SLAC), using the e^+e^- collider Standford Positron Electron Accelerating Ring (SPEAR). This particle was named J/ψ and at that time the

known quarks were up, down and strange, then the new particle consisted of the predicted quark species, the charm quark and a new fundamental particle were discovered.

1.3.1 Parity

The parity operator acts on a wave function inverting the direction of all spacial coordinates:

$$\Psi(\vec{r}) = \Psi(-\vec{r}) \tag{1.8}$$

and if we apply the parity operator twice, we get right back where we started:

$$P^2 = I \tag{1.9}$$

then the eigenvalues of P are ± 1.

Hadrons are eigensatates of P and they are classified according to their eigenvalue. Fermions must have an opossite parity of the corresponding antiparticle, then quarks are taken to have positive intrinsic parity, so the antiquarks are negative. Parity is a multiplicative quantum number and in the groundsate of a composite system, parity is the product of the parities of its constituents, then the groundstate of charmonia have negative parity $(-1)(+1)$. for excited states, there is a factor of $(-1)^l$ (here l is the orbital angular momentum), then in general mesons carry a parity of $(-1)^{l+1}$

1.3.2 Charge conjugation

Reminding the quarkonia discussion, charmonia states are neutraly charged, this means that the J/ψ particle is an eigenstate of charge conjugation operator C, then C changes the sign of all "internal" quantum numbers.

An intersting result for particles made up from a $\frac{1}{2}$ spin particle and its anti-

particle (just like the J/ψ meson we are studying) in a configuration with orbital angular momentum l and total spin S constitutes an eigensate of C, with the respective eigenvalue $(-1)^{l+S}$.

1.3.3 J/ψ Classification as a Polar Vector Meson

Once every quantum number of the charmonia bound state in the $l = 0$ state with $S = 1$ (refered as the J/ψ particle) We can use a most comun notation:

$$J^{PC} = 1^{--} \tag{1.10}$$

Where J, P, C are the total angular momentum, parity eigenvalue and charge parity eigenvalue of the system respectively.

A vector particle is an eigenstate of angular momentum operator with quantum number J=1 in natural units

$$\hat{J}^2 |V\rangle = J(J+1) |V\rangle \tag{1.11}$$

and a "polar" vector particle has negative parity.

This propriety allows the particle to be produced by annihilation of a quark and its antiquark, and to decay into a lepton-antilepton pair.

V can be any of three of the angular momentum components J_z allong a quantization axis z.

$$\hat{J}_z |V\rangle = M |V\rangle , \quad M = -1, 0, 1 \tag{1.12}$$

thus, we refer to the J/ψ particle as a polar vector meson.

1.4 J/ψ Polarization

Polarization of a vector particle refers to how the three base eigenstate are combined to form the observed state of V, This combination is determined by the production mechanism under the given experimental conditions.

Measuring a particle's polarization essentially means determining the average composition of its J_z states within the collected event sample. This measurement relies on the fact that the particle tends to emit its decay products on characteristics directions, wich are strongly related with its actual J_z projection.

By identifying many such decays, the experiment builds a statical distribution of the emission angles on the particle's rest frame. Analyzing the shape of this angular distribution then reveals the polarization of the particle.

1.4.1 Helicity conservation

Chirality of fermions is preserved by electromagnetic and strong forces, and the expression $u\gamma^\mu u = u_L\gamma^\mu u_L + u_R\gamma^\mu u_R$, describing the dynamics of the coupling of electrons to photons (where γ^μ are the Dirac matrices and u is the electron spinor), shows that terms containing both opposite chiral components (u_L and u_R for left-handed and right-handed chiral component) are absent, this means that the fermion chirality is preserved in the interaction with the photon.

In the massless fermion limit, left and rigt-handed chiral components become eigenstates of the helicity operator $h = \frac{S\cdot p}{|p|}$ (projection of the spin on the momentum direction). Under this condition, chirality conservation becomes helicity conservation.

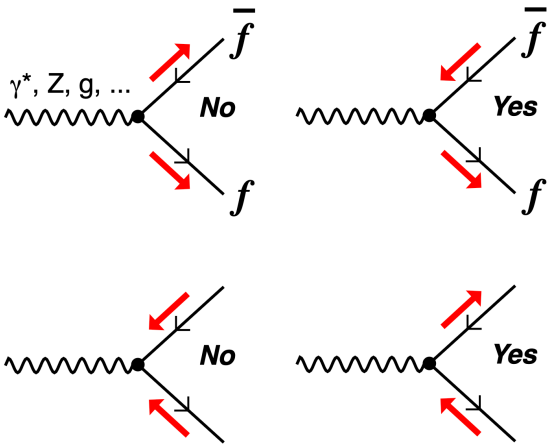


Figure 1.3: Diagram of helicity conservation in the decay of a gauge boson into a fermion-antifermion pair. Red arrows indicate the spin orientations of the outgoing f and $\bar{f}$ and the black arrows represent the direction of the fermion flux.

Helicity conservation implies opposite helicities in the fermion and antifermion resulting from the decay of a virtual photon (or another gauge boson) as the boson carries zero (fermion) helicity.

In the J/Ψ decay, where a charm and anti-charm quark annihilates into a virtual photon, resulting in the observed lepton anti-lepton pair, in the J/Ψ rest frame the leptons have anti-parallel momenta and to satisfy helicity conservation, they must have the same spin orientation. this consideration implies a total angular momentum in the z' axis is $L' = 1$ or -1, while the case $L' = 0$ is forbidden in this limit

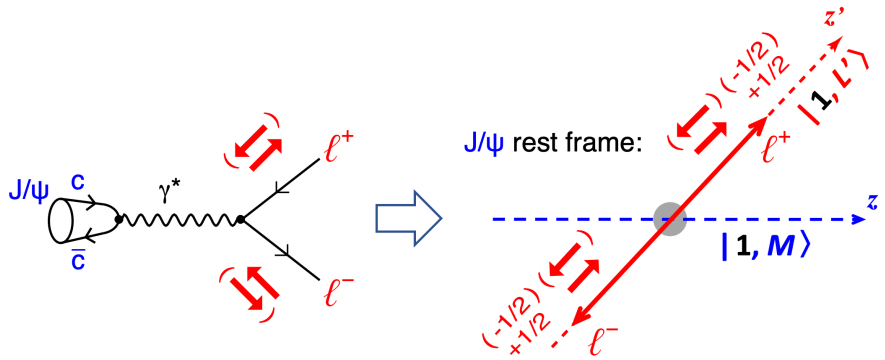


Figure 1.4: Helicity conservation in the decay J/Ψ in to lepton and anti-lepton pair (left) and the effect on the total angular momentum of the di lepton system as seen in the J/Ψ rest frame (right).

Then helicity conservation "polarizes" the dilepton system with maximal projection of angular momentum along the emission axis in the J/ψ rest frame. This property is related to the decay process, so we are not talking about any J/ψ polarization state yet because the polarization is measured in a chosen quantization axis related to the emission axis, as we will discuss later

1.4.2 Angular Distribution

The angular distribution is expressed in spherical coordinates with the polar angle θ being the angle between the direction of the positive charged lepton and the chosen z axis, and the azimuthal angle ϕ measured with respect to the zx plane [2], an illustration of the coordinate system is shown in Fig 1.5

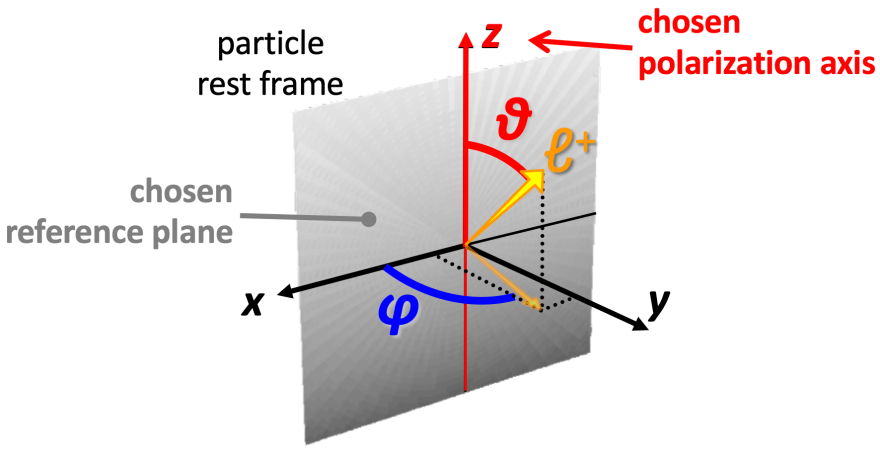


Figure 1.5: Coordinate system for measurement of a two body decay distribution, axes and angles are defined in the rest frame of the decaying particle

The analysis commences by examining a single production subprocess, wherein the J/ψ is formed as a defined superposition of the $J = 1$ eigenstates $J_z = +1, 0, -1$ relative to the polarization axis z.

$$|V\rangle = b_{+1}\,|+1\rangle + b_0\,|0\rangle + b_1\,|-1\rangle \tag{1.13}$$

Calculation of the angular distribution are performed in the J/ψ rest frame, where

the direction of the two leptons define the z' axis in Fig 1.6

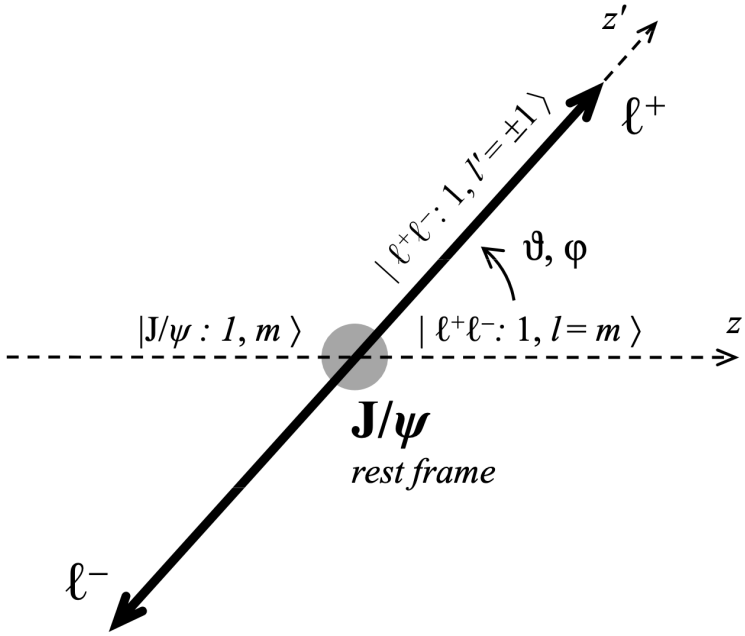


Figure 1.6: Sketch for the decay $J/\psi \to l^+l^-$, with the notation used for axis and angles in the J/ψ rest frame

The case we are treating with is the dilepton (final state) coupled to a photon in the process:

$$J/\psi \to \gamma^* \to l^+l^- \tag{1.14}$$

with angular projection ± 1 along the z' quantization axis, then we have an eigenstate of $J_{z'}|l^+l^-; 1, l\rangle$ and we want to express this state as a superposition of eigensates of J_z, $|l^+l^-; 1, l\rangle$ with $l = 0, \pm 1$.

This change of quantization axis is performed by rotating the quantization axis until it coincides with the one of the initial state:

$$|J, M'\rangle = \sum_{M=-J}^{+J} \mathcal{D}^J_{MM'}(\mathcal{R})|J, M\rangle. \tag{1.15}$$

The most general transformation performing this projection is parametrized with $\beta = \theta$ and $\alpha = -\gamma = \varphi$ and the dilepton angular momentum is expressed as

eigenvalues of J_z as [2]:

$$|l^+l^-;1,l'\rangle = \sum_{l=0,\pm1} \mathcal{D}^1_{ll'}(\varphi,\theta,-\varphi)|l^+l^-;1,l\rangle \tag{1.16}$$

As a general result, polarization in presence of n contributing production process, with $f^{(i)}$ weights, distribution can be expressed as[3]:

$$W(\cos\vartheta,\varphi) \propto \frac{\mathcal{N}}{(3+\lambda_\vartheta)}\big(1+\lambda_\vartheta\cos^2\vartheta+\lambda_\varphi\sin^2\vartheta\cos 2\varphi+\lambda_{\vartheta\varphi}\sin 2\vartheta\cos\varphi\big) \tag{1.17}$$

Then the observable shape parameter λ_θ is a weighted average of the corresponding parameters, $\lambda_\theta(i)$.

The simplified one dimensional analysis is often chosen for practical reasons in experimental measurements, characterizing the single sub processes and the angular distribution that will be used in this work for the angular distribution fit to extract the λ_θ parameter is:

$$W(\cos\vartheta,\varphi) \propto \frac{\mathcal{N}}{(3+\lambda_\vartheta)}\big(1+\lambda_\vartheta\cos^2\vartheta\big) \tag{1.18}$$

Chapter 2

LHC and ATLAS experiment

2.1 Large Hadron Collider

LHC is the world's larger and most powerful particle accelerator in CERN, located at the Franco-Swiss border near Geneva, Switzerland. It consists of a 27-kilometre ring of superconducting magnets with accelerating structures to boost the energy of the particles and It sits in a tunnel 100 meters underground.

Two high-energy particle beams travel in opposite directions in separate beam pipes (two tubes kept at ultrahigh vacuum) inside the detector almost at the speed of light before they collide. This particles are guide by a strong magnetic field, produced by superconducting electromagnets that must be at -271.3°C, that is the reason why much of the accelerator is connected to a distribution system of liquid helium.

There are nine experiments at lhc: ALICE, ATLAS, CMS, LHCb, LHCf, TOTEM, MoEDAL-MAPP, FASER.

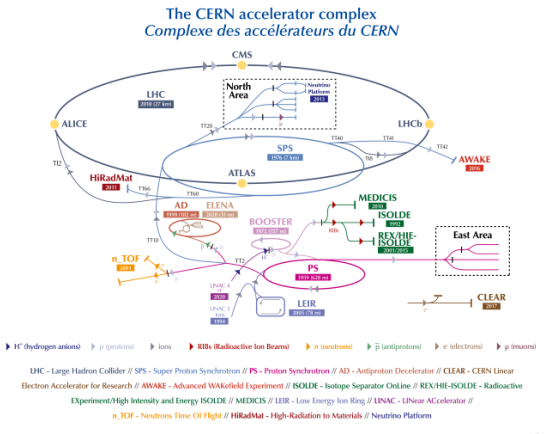


Figure 2.1: Schematics of CERN accelerator complex

2.2 ATLAS detector

ATLAS detector is a general-purpose particle physics experiment at the LHC to study from SM measurement to research for new physics. Is the largest collider detector ever built with 25 m in height and 44 m in length, and It covers a full 4π polar angle. This detector is made of four main sub-system with cylindrical symmetry around the interaction point (IP), with the inner most being the tracking system, also known as Inner Detector (ID). The next layers are rwo calorimeters, this systems are designed to measure the energy of the particles, and finally the Muon Spectrometer wich reconstruct the trajectory of Muons that scape from the calorimeter. A schematic of ATLAS detector is shown in Fig 2.2

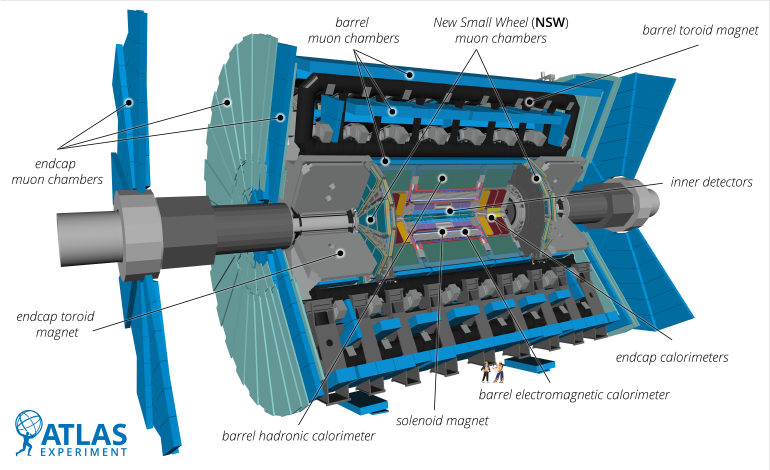


Figure 2.2: Atlas detector layout illustration

2.3 Coordinate system of the Atlas detector

The ATLAS detector uses a right-handed coordinate system (x, y, z) with the origin of the system placed at the interaction point. The z-axis is fixed along the beam pipe, the x-axis points from the IP to the center of the LHC ring, and the y-axis points upwards. Polar coordinates (r, ϕ, θ) are more common to express positions, with ϕ being the parameter that measures angular distance in a plane perpendicular to the beam direction (the $x - y$ transverse plane), in other words, ϕ is the azimuthal angle around the z-axis, θ is the angle that measures angular

distance from the z-axis and radial distance form the origin is given by r.

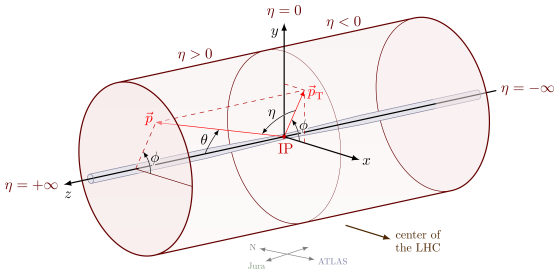


Figure 2.3: ATLAS coordinate system at LHC

Rapidity can be defined as:

$$y = \frac{1}{2} \ln \frac{E + p_z}{E - p_z} \tag{2.1}$$

wich is useful in high-energy particle collisions because It is related to the angle between the XY plane and the direction of emission of a product of the collision, but in practice, It can be difficult to measure both momentum and energy of the particle. There is a way of defining a quantity that is almost the same thing as the rapidity at high-energy collisions, This leads to the concept of pseudo–rapidity:

$$\eta = -\ln \tan \frac{\theta}{2} \tag{2.2}$$

wich gives a very useful relation between θ and η in the the context of this work.

2.4 Inner s

The ID is the detector closest to the interaction point, placed around the beam pipe and surrounded by a 2 T solenoid magnet; a schematic of the ID is shown in Fig. 2.4. The ID covers up to $|\eta| < 2.5$ with full coverage in ϕ and is made up of these sub-detectors:

1. Pixel Detector: The detector is made up of four layers of silicon pixel , is the first point of detection and It measures signals from charged particles who deposits small amounts of energy with a precision of almost 10 μm to reconstruct the origin and momentum of the particle.

2. Semiconductor Tracker (SCT): The SCT surrounds the Pixel Detector and It measures with high precision the trajectory of charged particles that come from the IP after collisions. The detector is composed of 4088 module of silicon-strip to measure particles track with a precision of 25 μm

3. Transition Radiation Tracker (TRT): The final layer of the inner detector, the TRT is composed of 300.000 'straws' filled with a gas mixture. charged particles cross straws and ionize the gas, creating a detectable electric signal providing information on the particle type that flew through the detector (i.e. an electron or pion).

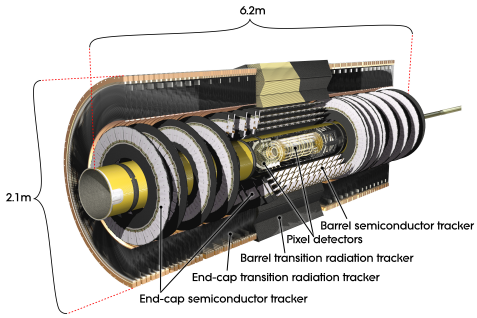


Figure 2.4: Computer generated image of the ATLAS inner detector

2.5 Calorimeters

after particles go through the inner detector system, the next layer of the ATLAS detector is composed of the calorimeters and these are formed of two interleaved layers; a passive material (the absorber), that fully stops the incoming charged and neutral particles (except neutrinos and high-pt muons) producing a shower of additional particles, and an active material that measures their energy.

This calorimeter system is divided into electromagnetic and hadron calorimeters (ECAL and HCAL respectively) which are described as follows:

- Electromagnetic calorimeters: ECAL is designed to measure particles with electromagnetic interactions, such as photons and electrons.

  the passive material is lead and the active material is liquid argon (LAr), known as the LAr calorimeter.

- Hadronic calorimeters: HCAL function is to measure the energy of hadrons, this system is divided into a barrel and two end-caps. The barrel consists of steel (the absorber) and plastic scintillator tiles (the active material), forming the Tile Calorimeter.

  The HCAL is designed with sufficient thickness to minimize pucnh-trough effects and to ensure an accurate measure of missing transverse energy.

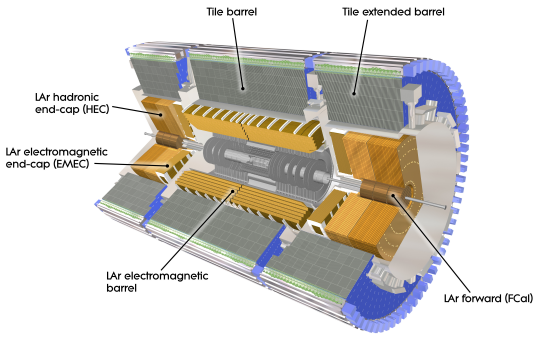


Figure 2.5: Ilustration of ATLAS calorimeter and different components of ECAL and HCAL

2.6 Muon Spectrometer

The outer layer of the ATLAS experiment is made of Muon detectors, the Muon spectrometer is the largest of the ATLAS sub-detectors and It identfy and measure the momenta of Muons with very high presicion, this particles are similar to electrons but 200 times heavier, this allows them to go troguh the thick layer of ATLAS calorimeters without being stopped. To track the trajectory of Muons

with high precision, Monitored Drift Tube (MDTs) detectors are used, these detectors are composed of 3 cm wide aluminum tubes filled with a gas mixture. Muons pass through the tubes, knocking electrons out of the gas, these particles travel to the wire located at the tube's center, where they produce a signal. 380.000 aluminum tubes are stacked up to several layers in order to measure the trajectory of Muons.

ATLAS uses fast-response detectors to select collisions events that are potentially useful for physics analysis. This desicion is made in 2.5 μs.

The Resistive Plate Chambers (RPCs) surround the central region of the ATLAS experiment and They are formed by two parallel plastic plates at a voltage difference, with a gas-filled space in between.

Thin Gap Chambers (TGCs) are ubicated at the ends of the ATLAS experiment and are made of 20 micro-meters wires in a gas mixture.

Both chambers detect Muons when they ionise the gas and produce a signal.

There are two additional detectors technologies designed for high-intensity LHC collisions, these detectors are Micromegas and Small-Strip Thin-Gap Chambers (sTGCs) and these can track muons in high-density areas close to the LHC beam pipe, quickly and with high precision. a schematic of the Muon spectrometer is shown in the external structure of Fig. 2.2.

2.7 Muon Reconstruction

Muon reconstruction is performed by information from ID, MS, and calorimeter systems. There are five main reconstruction strategies, defined by the muon category:

- Combined (CB): Combined muons are reconstructed/identified by a matching method between MS and ID tracks performing a combined track fit based on the ID and MS hits with the calorimeter energy loss taken into

consideration. Using the particle trajectory associated with the combined fit, the MS hits corresponding to the track may again be updated and the track fit repeated.

- Inside -out Combined (IO): IO muons are reconstructed with an Inside-out approach: an ID track is extrapolated into the muon spectrometer, where the algorithm searches for at least three MS hits that are roughly aligned with that projection. These MS hits, together with the ID track and the estimated energy loss at the calorimeters, are then used to perform a combined track fit. Because this method does not depend on a fully reconstructed MS track, it retains efficiency in areas with poor MS coverage and for low-pT muons that may not reach the middle MS station.

  If no ID track can be associated with an MS track, the MS track is extrapoled back to the beamline and its parameters are used to form an ME muon. These muons help extend the acceptance beyond the ID's coverage, allowing the full MS acceptance up to $|\eta| = 2.7$ to be utilized.

- segment-tagged(ST): ST muons are selected by requiring that an ID track, when extrapolated to the MS, matches at least one reconstructed MS segment within tight angular criteria. once such a match is found, the ID track is taken as the muon candidate, and its fitted parameters are used as the muon's kinematic values.

- calorimeter-tagged(CT): CT muons are reconstructed by projecting ID tracks outwards into the calorimeters and searching for energy deposits compatible with those of a minimum-ionising particle. When such a deposit is found, it is used to tag the ID track as a muon, and the muon kinematics are taken directly from the ID track fit.

  Unlike the other reconstruction algorithms, which accepts ID tracks down to 2 GeV, CT muon reconstruction imposes a higher pT threshold of 5 GeV

due to the significant background contribution at low pT

2.8 Muon Identification

Muon identifications in ATLAS combines ID and MS information and applies strict quality requirements to suppress background from hadron decays while keeping high efficiency for prompt muons. Variables such as the $\frac{q}{p}$ significance, ρ', and the normalized χ^2 test the consistency of ID and MS measurements. Minimum hits requirement ensure a robust momentum measurement. ATLAS defines several identification working points (Loose, Medium, Tight, HIgh-pT) to match different analysis strategies.

- Medium muons: designed to minimize reconstruction and calibration uncertainties and It uses only CB and ME muons. A loose requirement on the ID-MS momentum compatibility is applied to reduce hadron misidentification, specifically enforcing a $\frac{q}{p}$ significance below seven. For $|\eta| < 2.5$, about 0.5% of the medium muons come from the inside-out reconstruction.

- Loose muons: The loose muons identification aims to maximize reconstruction efficiency while ensuring good track quality. it include all muons type, and all CB and ME that satisfy de medium criteria are automatically accepted. CT and ST muons are only used in the $|\eta| < 0.1$ regions. For $|\eta| < 2.5$, about 97.5% of loose muons are combined muons, around 1.5% are CT and the remaining 1% are ST muons.

- Tight muons: The tight identification targets high-purity muon selection, sacrificing some efficiency. It uses only CB muons with hits in at least two MS stations and fulfilling the Medium criteria. The normalized χ^2 of the combined fit must be below 8 to reject poorly reconstructed tracks. Additionally, a two-dimensional cut in $\frac{q}{p}$ and ρ' significance, dependent on

pT, is applied to improve background rejection, especially for muons with pT$<$ 20Gev where misidentification rates are higher.

- High-pT muons: This selection is designed to maximize momentum resolution for muons with pT$>$ 100 GeV optimized for searches involving high-mass resonances. It uses CB muons that satisfy the Medium criteria and have hits in at least three MS stations. Regions of the MS with poor alignment are vetoed.

Chapter 3

Results

3.1 Di Muon Invariant Mass Spectrum in Heavy Ions Collisions

Six resonance picks are observed in the Dimuon invariant mass spectrum in the range of 0-100 GeV corresponding to the ω, ϕ, J/ψ, $\psi(2S)$, Υ, and the Z boson. Υ has three states $\Upsilon(1S)$, $\Upsilon(2S)$, and $\Upsilon(3S)$ but it shows as an individual pick in the spectrum. Some of the validation plots made by ATLAS are shown below.

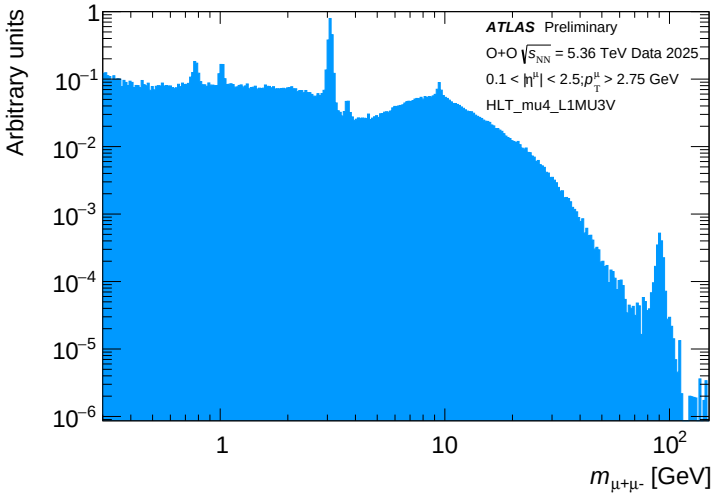


Figure 3.1: Dimuon invariant mass spectrum in O+O collisions at $\sqrt{S_{NN}} = 5.36$ TeV recorded in 2025. The distribution is shown for muons passing p_T >2.75 GeV and $0 < |\eta| < 2.5$ and selected using the trigger HLT_mu3_L1MU3V. The histogram is scaled to unit integral. The distribution was built by combining each negatively charged muon with each positively charged muon in a given event, resulting in a combinatorial background.

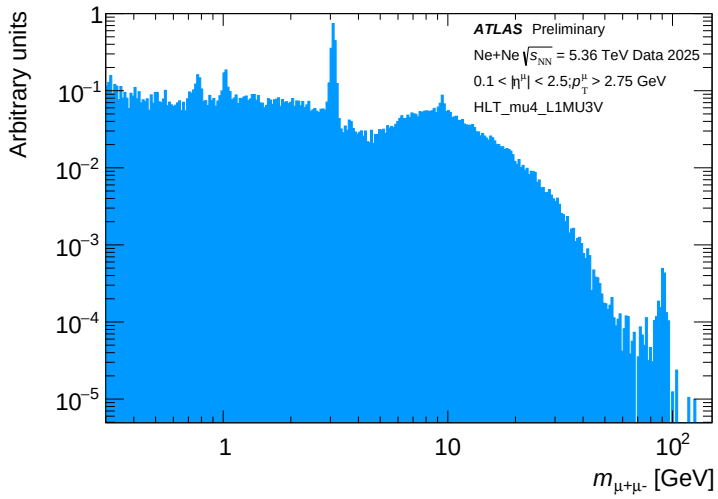


Figure 3.2: Dimuon invariant mass spectrum in Ne+Ne collisions at $\sqrt{S_{NN}} = 5.36$ TeV recorded in 2025. The distribution is shown for muons passing p_T >2.75 GeV and $0 < |\eta| < 2.5$ and selected using the trigger HLT_mu3_L1MU3V. The histogram is scaled to unit integral. The distribution was built by combining each negatively charged muon with each positively charged muon in a given event, resulting in a combinatorial background.

These results correspond to 2025 collisions, during which 0+0 and Ne+Ne collisions were performed for the first time. In these collisions, the Z boson resonance was observed for the first time in this specific collision type. We obtained these plots in July 2025, and they are publicly available in the Heavy Ion Trigger Public Results

3.2 λ_θ Measurement for J/ψ Polarization

In the following section, we present the results of fitting the theoretical angular distribution to the cos(θ) distribution, where, as previously mentioned, θ is the angle between the emission axis of the positive muon μ^+ and the axis perpendicular to the Event Plane. The data have been filtered by centrality to observe the effects on polarization within a pT range of 8-24 GeV, in 2 GeV bins.

The solid blue line represents the theoretical fit and red lines show Null Hypothesis, with zero polarization.

3.2.1 J/ψ Candidates

For the J/ψ reconstruction, the di muon invariant mass spectrum was calculated on an event by event basis, taking in to account the efficiency criteria applied to each individual muon, and there for to the di muon system, as well as the event plane, which will be defined and explained below. The $J\psi$ candidates are selected in the di muon channel:

$$J/\psi \to \mu^+\mu^- \tag{3.1}$$

with

$$\mathcal{B}(J/\psi \to \mu^+\mu^-) = \frac{\Gamma(J/\psi \to \mu^+\mu^-)}{\Gamma_{total}(J/\psi)} = (5.961 \pm 0.033)\% \tag{3.2}$$

In each event, muons with opposite charge are combined to get the dimuon invariant mass, generating a combinatorial background. The condition to every dimuon pair to be classified as a J/ψ candidate is:

$$|m_{\mu^+\mu^-} - M_{J/\psi}| < 0.3\text{GeV} \tag{3.3}$$

where $M_{J/\psi} = 3096.900 \pm 0.006$.

It is important to mention that every individual muon has a pT cut of the form pT $>$ 4GeV and each dimuon (J/ψ candidate) have a rapidity cut $|y| < 2.0$.

$M_{J/\psi}$ and $\mathcal{B}(J/\psi \to \mu^+\mu^-)$ are obtained from the Particle Data Group 2025 update [4].

3.2.2 Event Plane

The Reaction Plane (RP) is the plane formed by the impact parameter "b" and the collisions axis. For central collisions b = 0 and RP can not be defined.

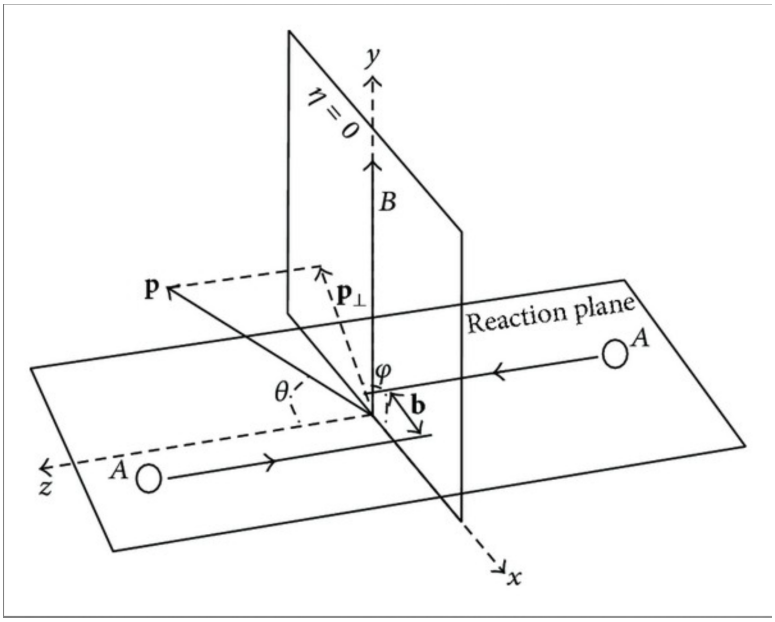


Figure 3.3: Schematic Diagram of reaction plane

In practice RP can not be be find but it can be approximated, this approximatio is known as "Event Plane". Event plane is estimated in the following way:

$$\Psi_2 = \frac{1}{2}\tan^{-1}\left(\frac{Q_{2,y}}{Q_{2,x}}\right) \tag{3.4}$$

with $Q_{2,x} = \sum_i \cos(2\phi_i)$ and $Q_{2,y} = \sum_i \sin(2\phi_i)$.

Here Ψ_2 is the second harmonic symmetry plane of charged particles at mid rapidity, $Q_{2,x}$ and $Q_{2,y}$ are the transverse components of the flow vector Q_2, finally, ϕ_i is the azimuthal angle of the i-th particle (or tracklet) used for the plane reconstruction. Polarization measurements for the J/ψ are performed with respect to the axis perpendicular of the event plane

3.2.3 Centrality

Centrality quantifies the overlap region of the two colliding nuclei and is related to the collision's impact parameter, being the transverse distance between the centers of the two nuclei at closest approach. Centrality is often expressed in percentages to indicate the degree of overlap. For example

- 0-10%: Collisions with the highest centrality involve maximum nuclear overlap, effectively simulating high-pileup environments where interactions are confined to a dense region. This maximizes the generated energy density and consequently yields the most expansive QGP volumes.

- 30-50%: Collisions considered more peripheral demonstrate reduced overlap and achieve a diminished energy density. Consequently, the resulting interaction dynamics in these events begin to approximate those characteristic of proton-proton interactions.

in this study, various centrality cuts are applied to differentiate the J/ψ polarization originating from central, semi-central, or peripheral events. To implement these cuts, the energy deposited in the calorimeter is restricted. A higher energy deposition (on the order of TeV) indicates a more central collision. This methodology allows us to investigate the influence of Quark Gluon Plasma (QGP) formation on the measured polarization relative to the event plane.

3.2.4 $0.1 - 20\%$ Centrality

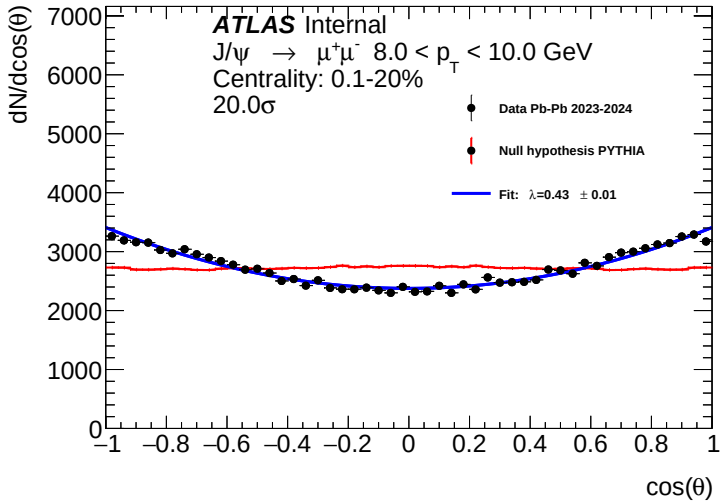


Figure 3.4: Angular distribution of $J/\psi \to \mu^+\mu^-$ candidates as a function of $\cos(\theta)$ in the centrality region 0.1-20% and in the transverse momentum range of $8 < \mathrm{pT} < 10$ GeV, with $\lambda_\theta = 0.43 \pm 0.01$ and a hypothesis test result of 20 σ

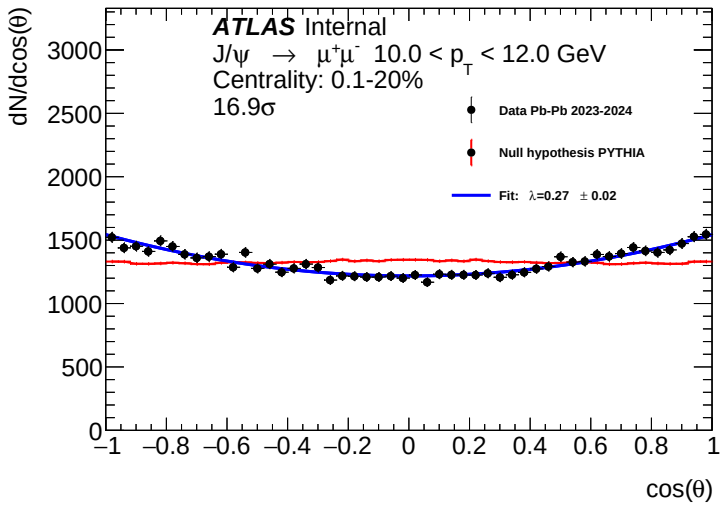


Figure 3.5: Angular distribution of $J/\psi \to \mu^+\mu^-$ candidates as a function of $\cos(\theta)$ in the centrality region 0.1-20% and in the transverse momentum range of $10 < \mathrm{pT} < 12$ GeV, with $\lambda_\theta = 0.27 \pm 0.02$, and a hypothesis test result of 16.9 σ

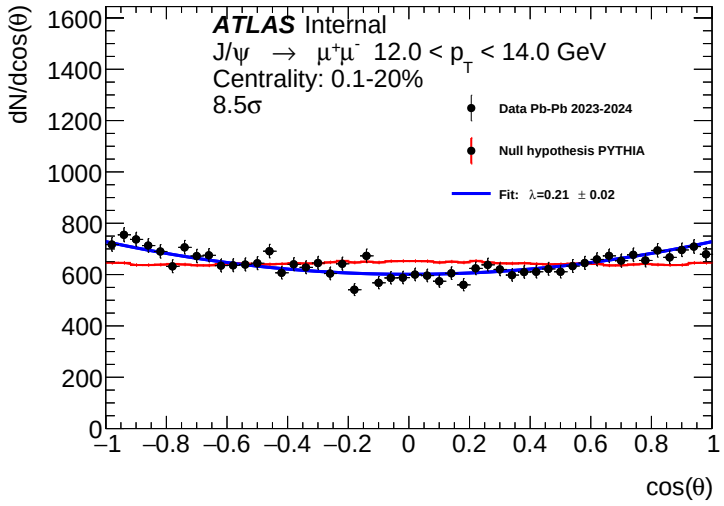


Figure 3.6: Angular distribution of $J/\psi \to \mu^+\mu^-$ candidates as a function of $\cos(\theta)$ in the centrality region 0.1-20% and in the transverse momentum range of $12 < \mathrm{pT} < 14$ GeV, with $\lambda_\theta = 0.21 \pm 0.02$, and a hypothesis test result of 8.5 σ

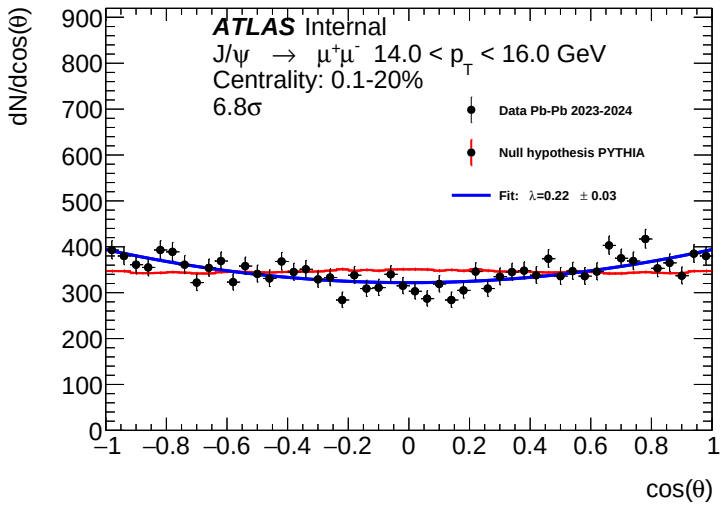


Figure 3.7: Angular distribution of $J/\psi \to \mu^+\mu^-$ candidates as a function of $\cos(\theta)$ in the centrality region 0.1-20% and in the transverse momentum range of $14 < \mathrm{pT} < 16$ GeV, with $\lambda_\theta = 0.22 \pm 0.03$, and a hypothesis test result of 6.8 σ

3.2.5 20-40% Centrality

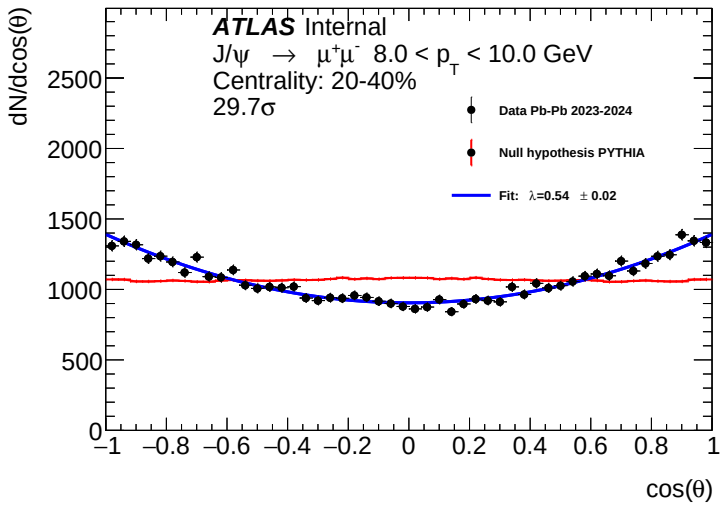


Figure 3.8: Angular distribution of $J/\psi \to \mu^+\mu^-$ candidates as a function of $\cos(\theta)$ in the centrality region 20-40% and in the transverse momentum range of $8 < \mathrm{pT} < 10$ GeV, with $\lambda_\theta = 0.54 \pm 0.02$, and a hypothesis test result of 29.7 σ

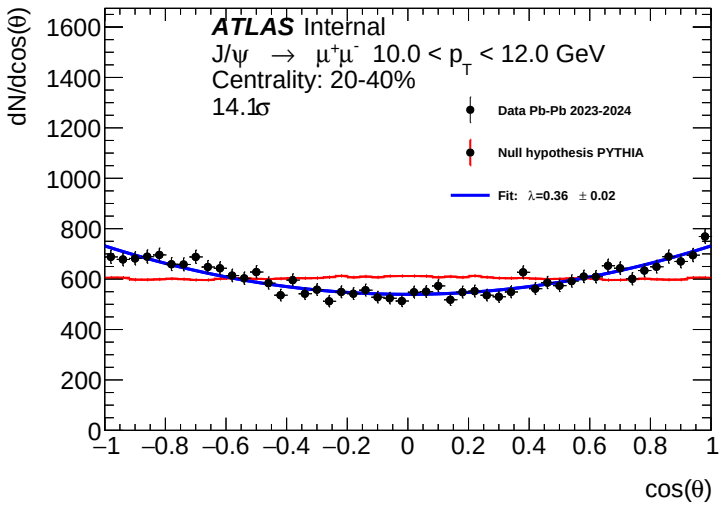


Figure 3.9: Angular distribution of $J/\psi \to \mu^+\mu^-$ candidates as a function of $\cos(\theta)$ in the centrality region 20-40% and in the transverse momentum range of $10 < \mathrm{pT} < 12$ GeV, with $\lambda_\theta = 0.36 \pm 0.02$, and a hypothesis test result of 14.1 σ

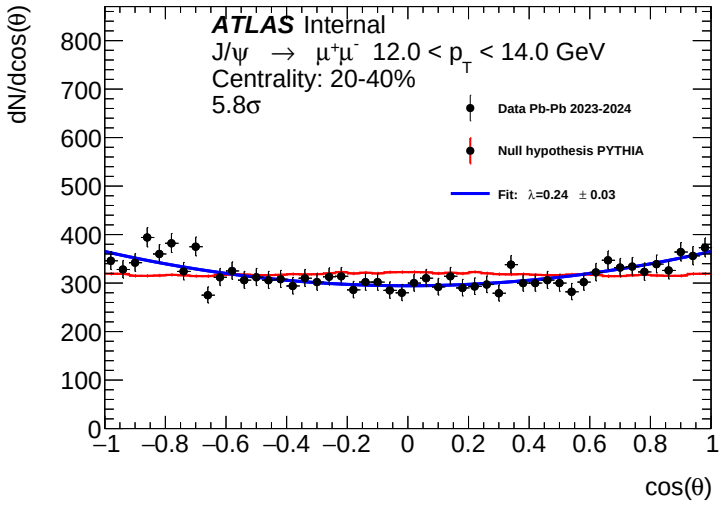


Figure 3.10: Angular distribution of $J/\psi \to \mu^+\mu^-$ candidates as a function of $\cos(\theta)$ in the centrality region 20-40% and in the transverse momentum range of $12 < \mathrm{pT} < 14$ GeV, with $\lambda_\theta = 0.24 \pm 0.03$, and a hypothesis test result of 5.8 σ

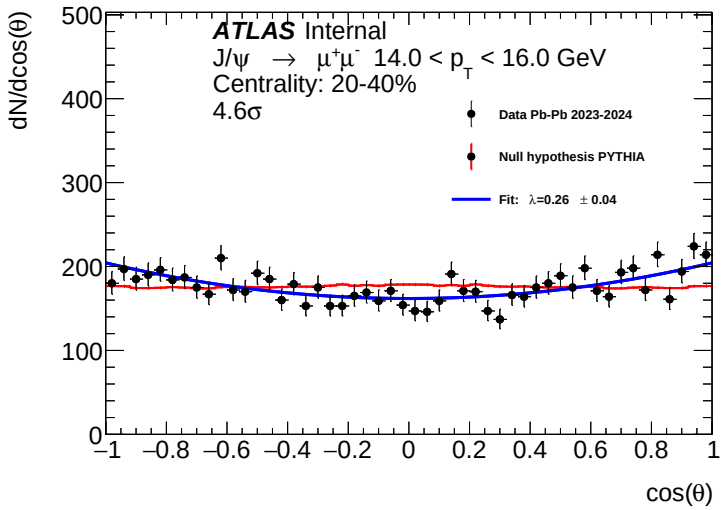


Figure 3.11: Angular distribution of $J/\psi \to \mu^+\mu^-$ candidates as a function of $\cos(\theta)$ in the centrality region 20-40% and in the transverse momentum range of $14 < \mathrm{pT} < 16$ GeV, with $\lambda_\theta = 0.26 \pm 0.04$, and a hypothesis test result of 4.6 σ

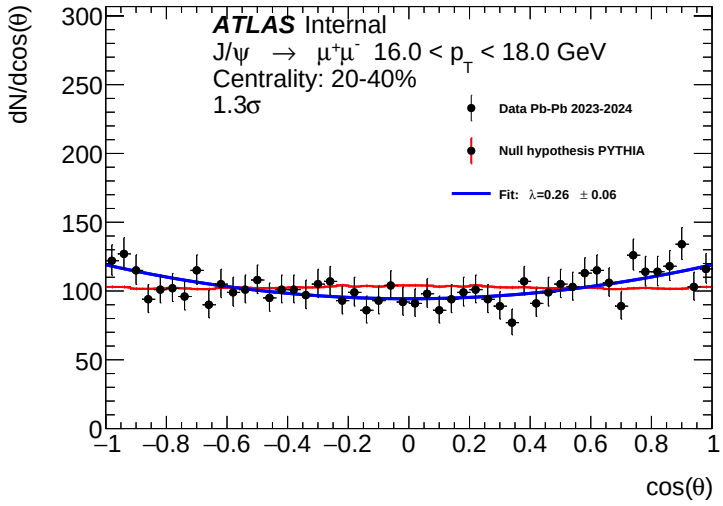


Figure 3.12: Angular distribution of $J/\psi \to \mu^+\mu^-$ candidates as a function of $\cos(\theta)$ in the centrality region 20-40% and in the transverse momentum range of $16 < \mathrm{pT} < 18$ GeV, with $\lambda_\theta = 0.26 \pm 0.06$, and a hypothesis test result of 1.3 σ

3.2.6 40-60% Centrality

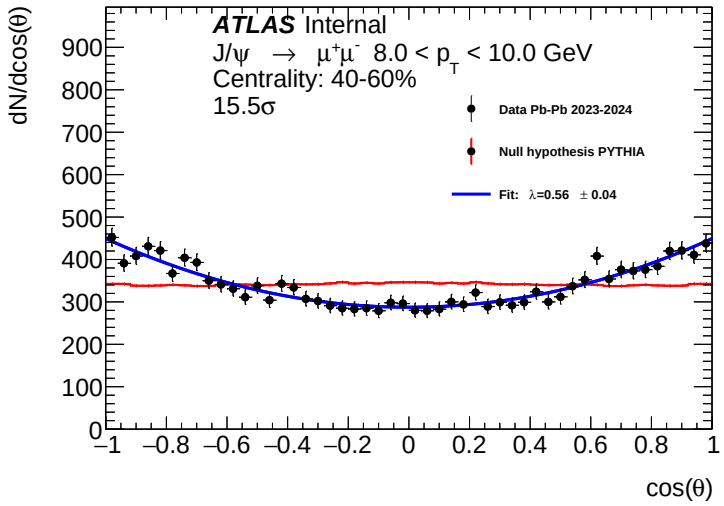


Figure 3.13: Angular distribution of $J/\psi \to \mu^+\mu^-$ candidates as a function of $\cos(\theta)$ in the centrality region 40-60% and in the transverse momentum range of $8 < \mathrm{pT} < 10$ GeV, with $\lambda_\theta = 0.56 \pm 0.04$, and a hypothesis test result of 15.5 σ

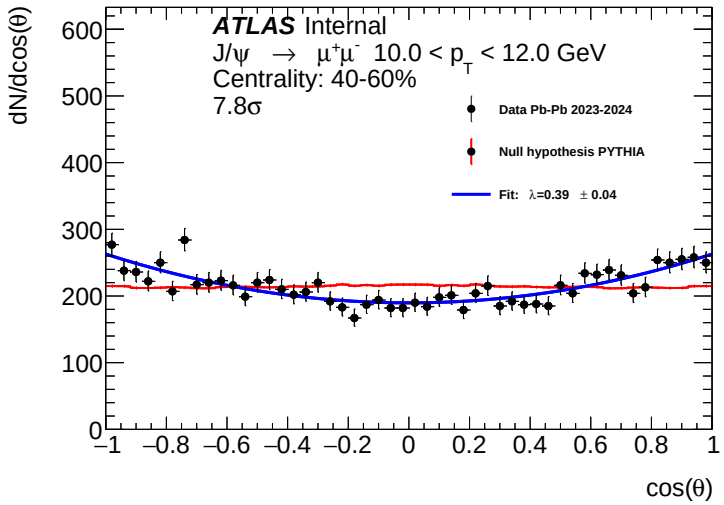


Figure 3.14: Angular distribution of $J/\psi \to \mu^+\mu^-$ candidates as a function of $\cos(\theta)$ in the centrality region 40-60% and in the transverse momentum range of $10 < \mathrm{pT} < 12$ GeV, with $\lambda_\theta = 0.39 \pm 0.04$, and a hypothesis test result of 7.8 σ

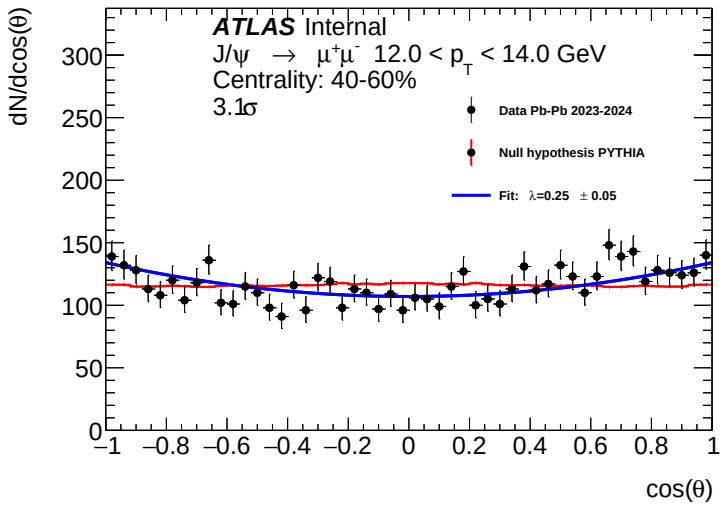


Figure 3.15: Angular distribution of $J/\psi \to \mu^+\mu^-$ candidates as a function of $\cos(\theta)$ in the centrality region 40-60% and in the transverse momentum range of $12 < \mathrm{pT} < 14$ GeV, with $\lambda_\theta = 0.25 \pm 0.05$, and a hypothesis test result of 3.1 σ

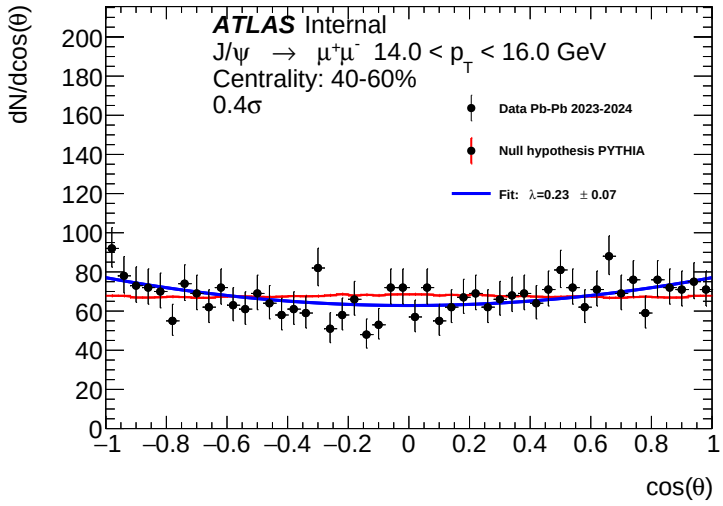


Figure 3.16: Angular distribution of $J/\psi \to \mu^+\mu^-$ candidates as a function of $\cos(\theta)$ in the centrality region 40-60% and in the transverse momentum range of $14 < \mathrm{pT} < 16$ GeV, with $\lambda_\theta = 0.23 \pm 0.07$, and a hypothesis test result of 0.4 σ

3.2.7 60-85% Centrality

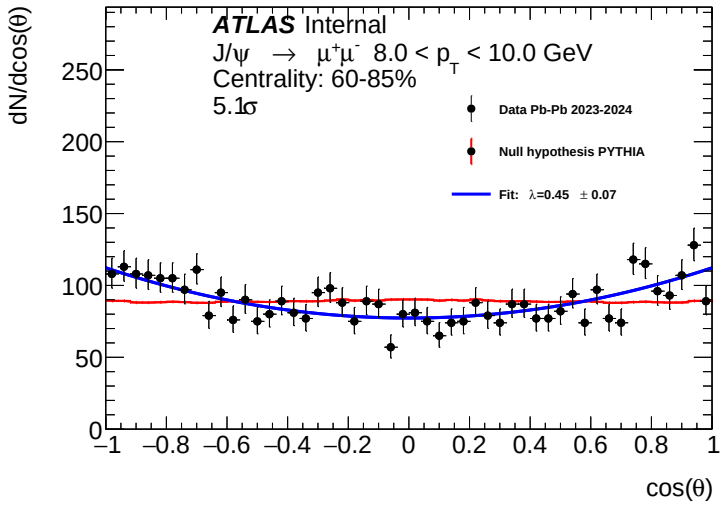


Figure 3.17: Angular distribution of $J/\psi \to \mu^+\mu^-$ candidates as a function of $\cos(\theta)$ in the centrality region 60-85% and in the transverse momentum range of $8 < \mathrm{pT} < 10$ GeV, with $\lambda_\theta = 0.45 \pm 0.07$, and a hypothesis test result of 5.1 σ

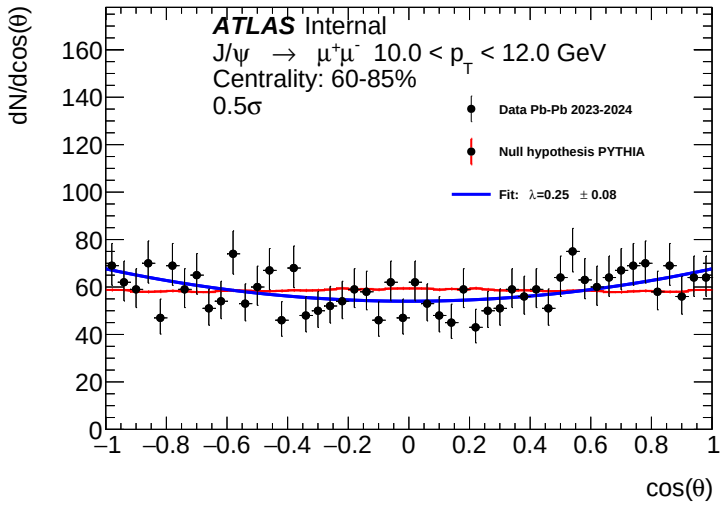


Figure 3.18: Angular distribution of $J/\psi \to \mu^+\mu^-$ candidates as a function of $\cos(\theta)$ in the centrality region 60-85% and in the transverse momentum range of $10 < \mathrm{pT} < 12$ GeV, with $\lambda_\theta = 0.25 \pm 0.08$, and a hypothesis test result of 0.5 σ

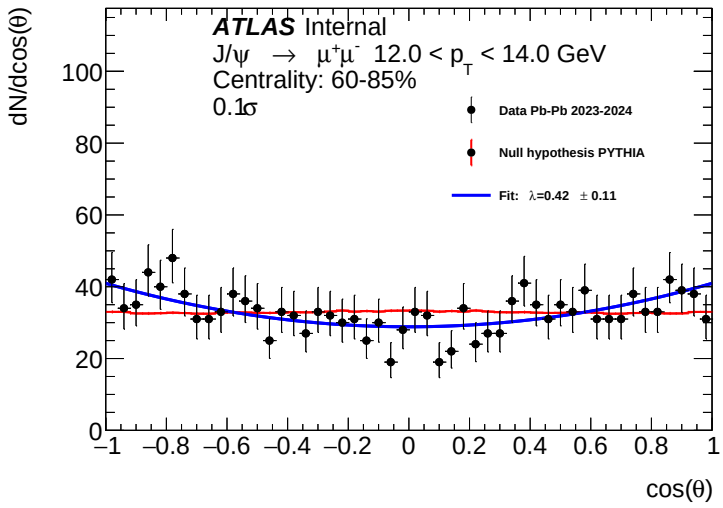


Figure 3.19: Angular distribution of $J/\psi \to \mu^+\mu^-$ candidates as a function of $\cos(\theta)$ in the centrality region 60-85% and in the transverse momentum range of $12 < \mathrm{pT} < 14$ GeV, with $\lambda_\theta = 0.42 \pm 0.11$, and a hypothesis test result of 0.1 σ

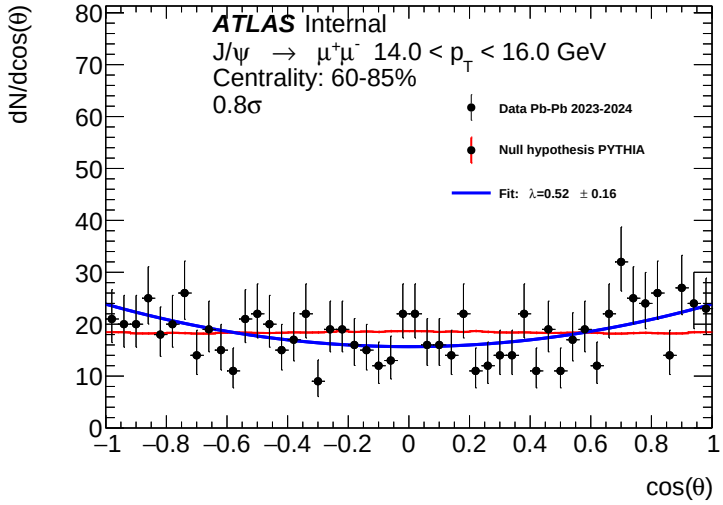


Figure 3.20: Angular distribution of $J/\psi \to \mu^+\mu^-$ candidates as a function of $\cos(\theta)$ in the centrality region 60-85% and in the transverse momentum range of $14 < \mathrm{pT} < 16$ GeV, with $\lambda_\theta = 0.52 \pm 0.16$, and a hypothesis test result of 0.8 σ

The λ_θ parameter extracted from each fit exhibits a decereasing trend as the pT increase grows. This clear tendency persists up to the forward pT range of 16-18 GeV where a lower number of events is available. Consequently, due to Poisson statistics, where the statistical uncertainty scales as $\frac{1}{\sqrt{N}}$, the error increases significantly in this range, making the λ_θ value less reliable. Nevertheless, the current statistics indicate a trend toward a flatter distribution. The situation is

somewhat similar when increasing the centrality ranges, as there is higher statistics in the more central collisions (larger number of events). However, unlike the previous analysis, the λ_θ value generally increases as the collision centrality decreases. This trend holds true until the pT range of 16-18 GeV is reached again, where for lower centralities, the angular distribution begins to align more closely with a flatter distribution given the current statistics in those ranges.

3.3 Backup

These results are taken from analysis regions that suffer from limited statistics, resulting in a significant uncertainty in the measured λ_θ values. Despite this, they are included as part of this study and are presented to provide validation and explore the phenomena present in these pT and centrality regimes with the current data set.

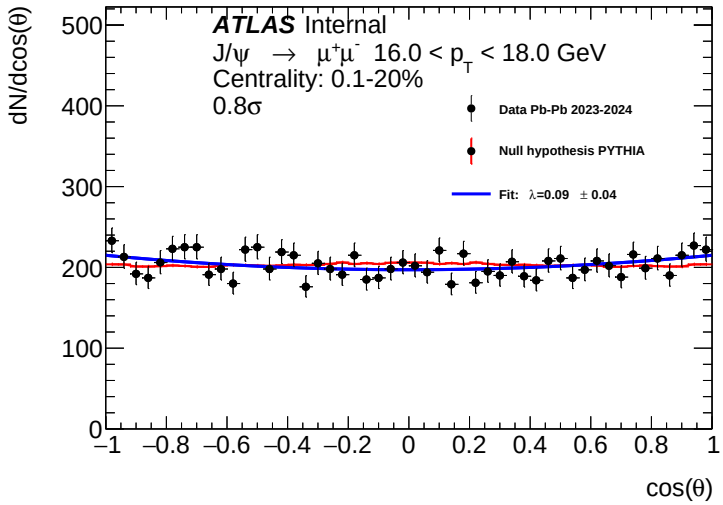


Figure 3.21: Angular distribution of $J/\psi \to \mu^+\mu^-$ candidates as a function of $\cos(\theta)$ in the centrality region 0.1-20% and in the transverse momentum range of $16 < \text{pT} < 18$ GeV, with $\lambda_\theta = 0.09 \pm 0.04$, and a hypothesis test result of 0.8 σ

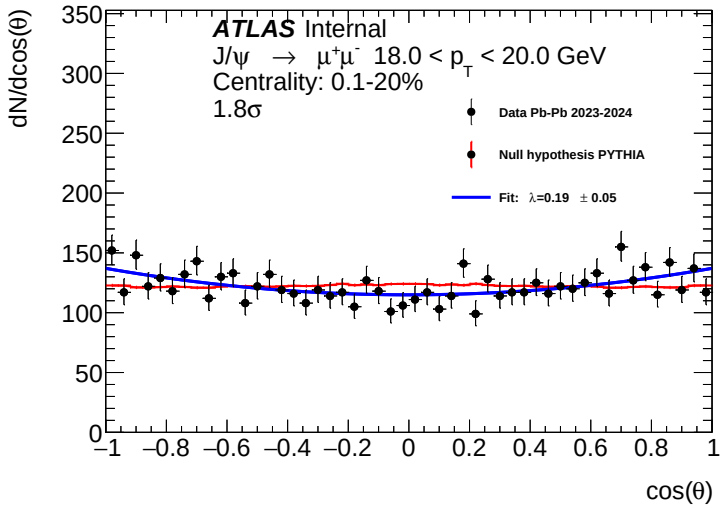


Figure 3.22: Angular distribution of $J/\psi \to \mu^+\mu^-$ candidates as a function of $\cos(\theta)$ in the centrality region 0.1-20% and in the transverse momentum range of $18 < \mathrm{pT} < 20$ GeV, with $\lambda_\theta = 0.19 \pm 0.05$, and a hypothesis test result of 1.8 σ

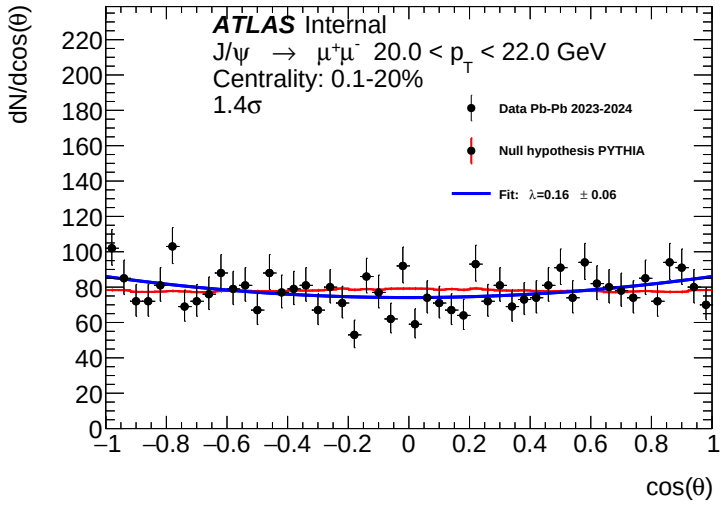


Figure 3.23: Angular distribution of $J/\psi \to \mu^+\mu^-$ candidates as a function of $\cos(\theta)$ in the centrality region 0.1-20% and in the transverse momentum range of $20 < \mathrm{pT} < 22$ GeV, with $\lambda_\theta = 0.16 \pm 0.06$, and a hypothesis test result of 1.4 σ

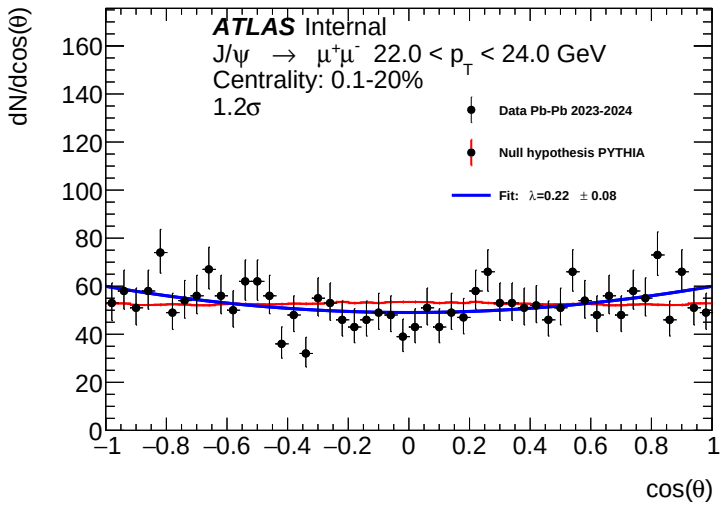


Figure 3.24: Angular distribution of $J/\psi \to \mu^+\mu^-$ candidates as a function of $\cos(\theta)$ in the centrality region 0.1-20% and in the transverse momentum range of $22 < \mathrm{pT} < 24$ GeV, with $\lambda_\theta = 0.22 \pm 0.08$, and a hypothesis test result of 1.2 σ

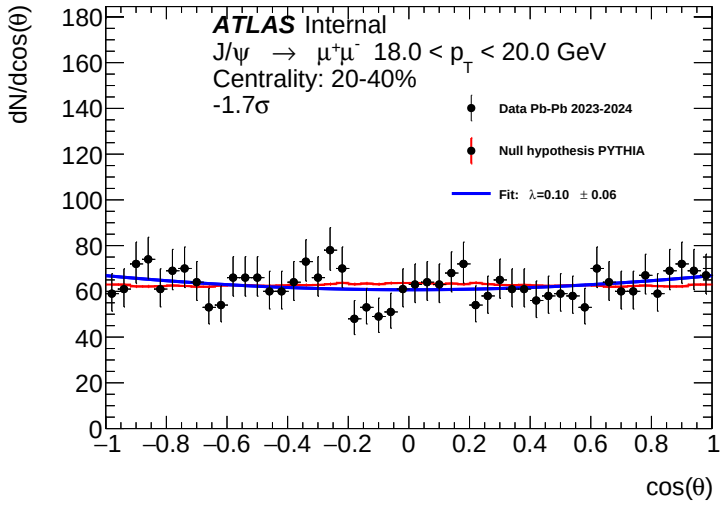


Figure 3.25: Angular distribution of $J/\psi \to \mu^+\mu^-$ candidates as a function of $\cos(\theta)$ in the centrality region 20-40% and in the transverse momentum range of $18 < \mathrm{pT} < 20$ GeV, with $\lambda_\theta = 0.10 \pm 0.06$, and a hypothesis test result of -1.7 σ

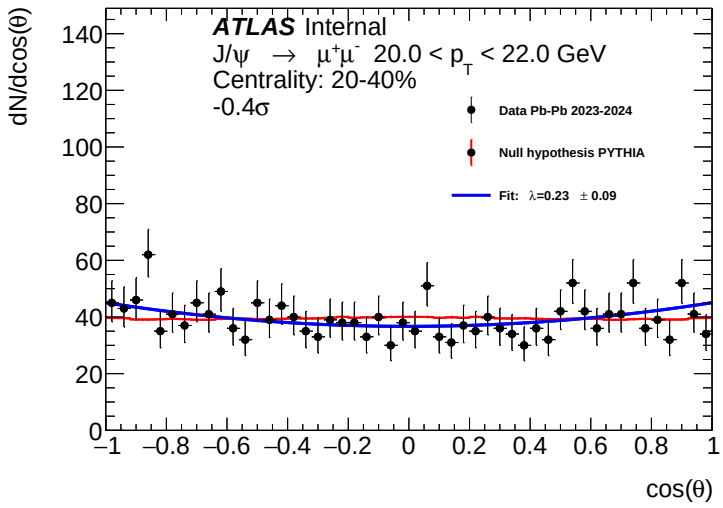


Figure 3.26: Angular distribution of $J/\psi \to \mu^+\mu^-$ candidates as a function of $\cos(\theta)$ in the centrality region 20-40% and in the transverse momentum range of $20 < \mathrm{pT} < 22$ GeV, with $\lambda_\theta = 0.23 \pm 0.09$, and a hypothesis test result of -0.4 σ

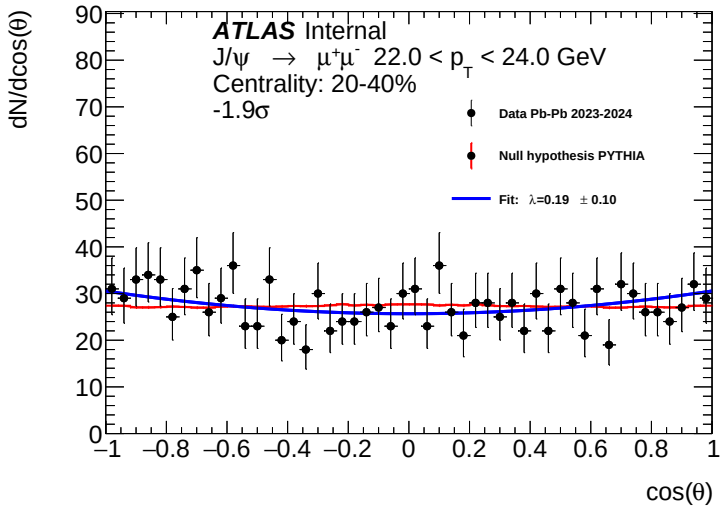


Figure 3.27: Angular distribution of $J/\psi \to \mu^+\mu^-$ candidates as a function of $\cos(\theta)$ in the centrality region 20-40% and in the transverse momentum range of $22 < \mathrm{pT} < 24$ GeV, with $\lambda_\theta = 0.19 \pm 0.10$, and a hypothesis test result of -1.9 σ

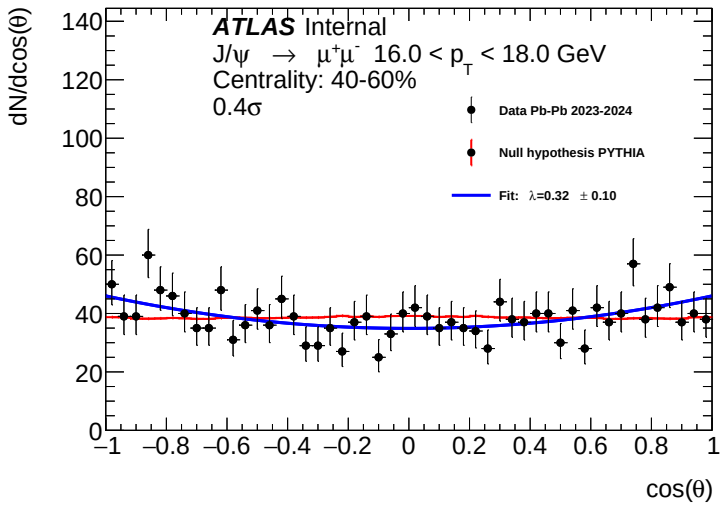


Figure 3.28: Angular distribution of $J/\psi \to \mu^+\mu^-$ candidates as a function of $\cos(\theta)$ in the centrality region 40-60% and in the transverse momentum range of $16 < \mathrm{pT} < 18$ GeV, with $\lambda_\theta = 0.32 \pm 0.10$, and a hypothesis test result of 0.4 σ

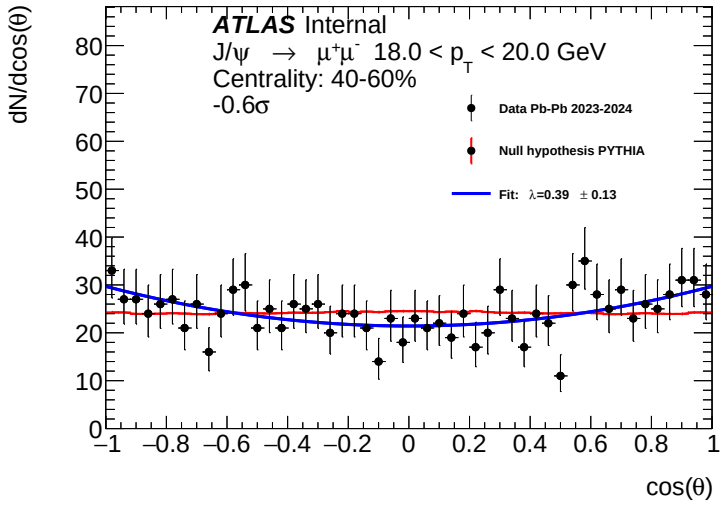


Figure 3.29: Angular distribution of $J/\psi \to \mu^+\mu^-$ candidates as a function of $\cos(\theta)$ in the centrality region 40-60% and in the transverse momentum range of $18 < \mathrm{pT} < 20$ GeV, with $\lambda_\theta = 0.39 \pm 0.13$, and a hypothesis test result of -0.6 σ

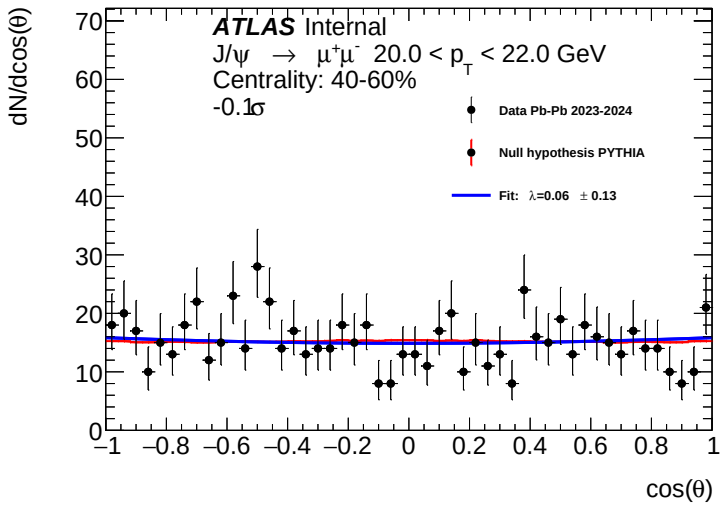


Figure 3.30: Angular distribution of $J/\psi \to \mu^+\mu^-$ candidates as a function of $\cos(\theta)$ in the centrality region 40-60% and in the transverse momentum range of $20 < \mathrm{pT} < 22$ GeV, with $\lambda_\theta = 0.06 \pm 0.13$, and a hypothesis test result of -0.1 σ

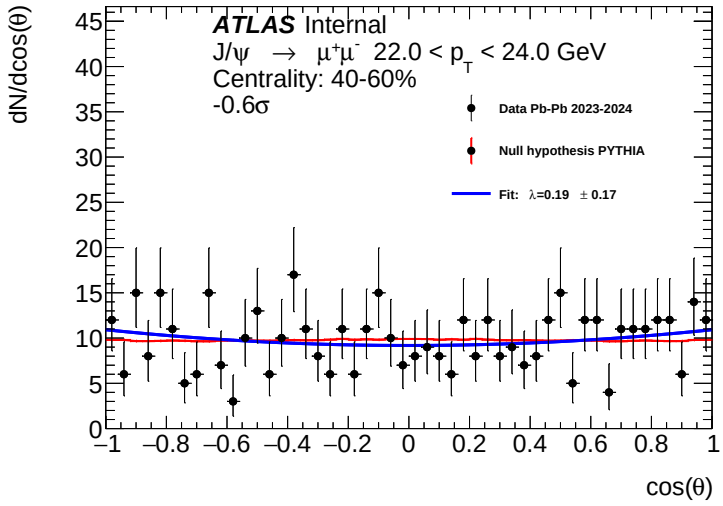


Figure 3.31: Angular distribution of $J/\psi \to \mu^+\mu^-$ candidates as a function of $\cos(\theta)$ in the centrality region 40-60% and in the transverse momentum range of $22 < \mathrm{pT} < 24$ GeV, with $\lambda_\theta = 0.19 \pm 0.17$, and a hypothesis test result of -0.6 σ

As can be observed, there are instances of negative σ values. This phenomenon occurs when a certain limit in the p-value magnitude of the hypothesis test is crossed. Nevertheless, the statistics are currently insufficient to consider this a critical issue, primarily due to the large disparity in event numbers between the simulated dataset (PYTHIA) and the data obtained from the real collisions.

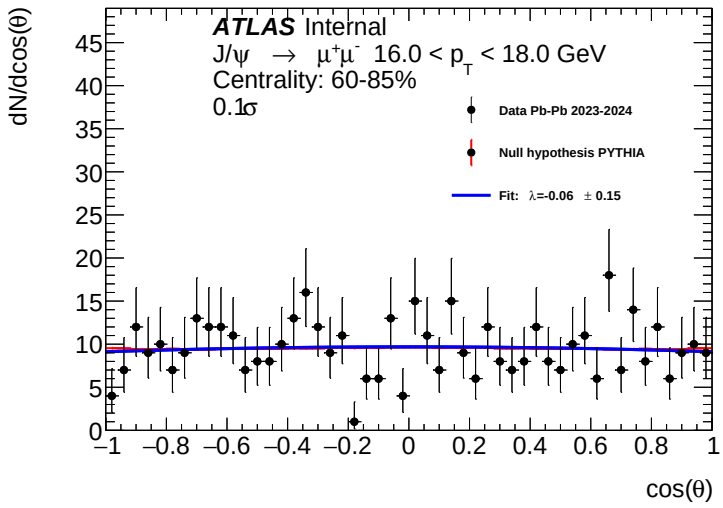


Figure 3.32: Angular distribution of $J/\psi \to \mu^+\mu^-$ candidates as a function of $\cos(\theta)$ in the centrality region 60-85% and in the transverse momentum range of $16 < \mathrm{pT} < 18$ GeV, with $\lambda_\theta = -0.06 \pm 0.15$, and a hypothesis test result of 0.8 σ

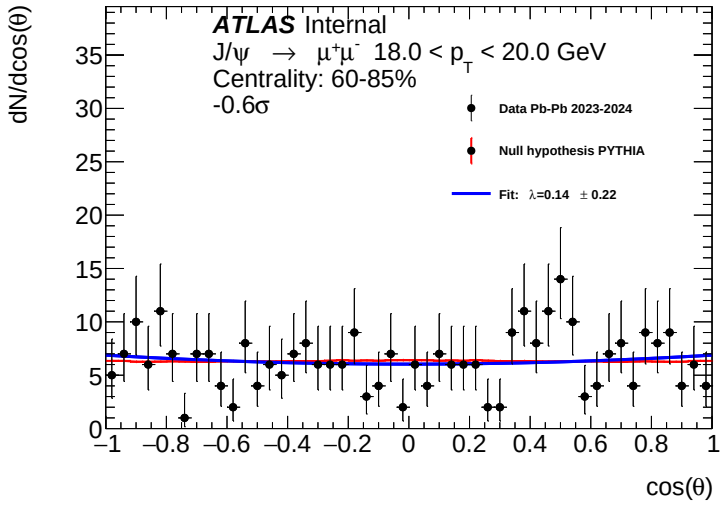


Figure 3.33: Angular distribution of $J/\psi \to \mu^+\mu^-$ candidates as a function of $\cos(\theta)$ in the centrality region 60-85% and in the transverse momentum range of $18 < \mathrm{pT} < 20$ GeV, with $\lambda_\theta = 0.14 \pm 0.22$, and a hypothesis test result of -0.6 σ

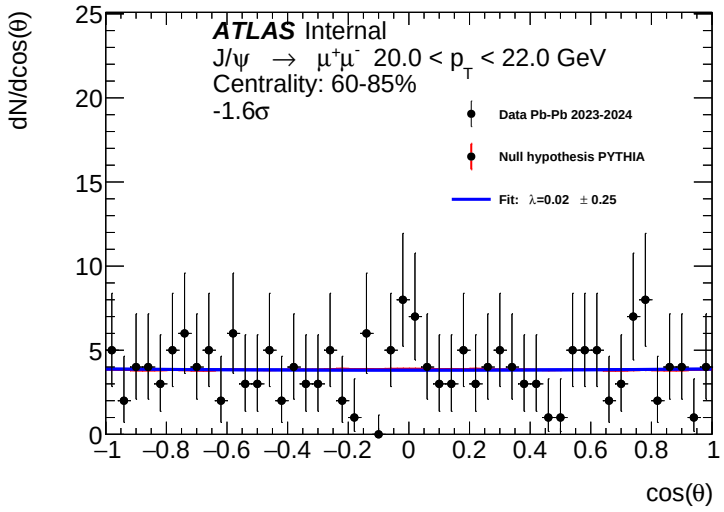


Figure 3.34: Angular distribution of $J/\psi \to \mu^+\mu^-$ candidates as a function of $\cos(\theta)$ in the centrality region 60-85% and in the transverse momentum range of $20 < \mathrm{pT} < 22$ GeV, with $\lambda_\theta = 0.02 \pm 0.25$, and a hypothesis test result of -1.6 σ

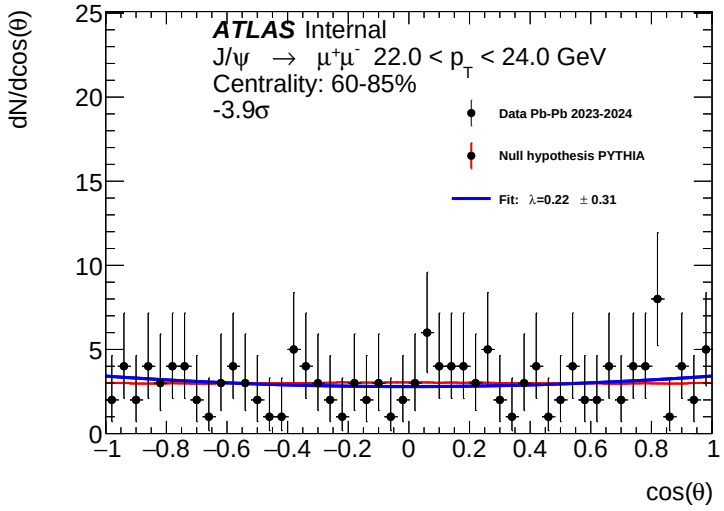


Figure 3.35: Angular distribution of $J/\psi \to \mu^+\mu^-$ candidates as a function of $\cos(\theta)$ in the centrality region 60-85% and in the transverse momentum range of $22 < \mathrm{pT} < 24$ GeV, with $\lambda_\theta = 0.22 \pm 0.31$, and a hypothesis test result of -3.9 σ

3.4 pT dependence of λ_θ

All the information obtained from the previous subsections can be analyzed in the next figure:

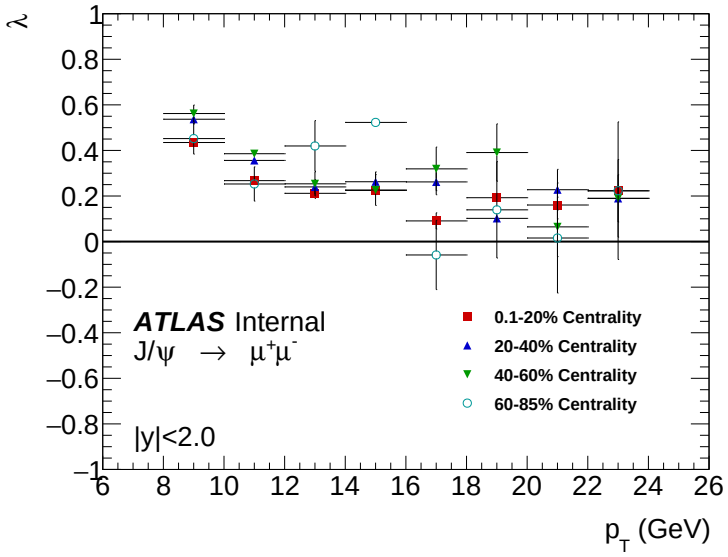


Figure 3.36: pT dependence of λ_θ, horizontal bars show the size of the pT ranges, with the data points being located at the center of each range, with different values of λ_θ for each centrality range.

The λ_θ parameter is observed to increase from central to semi-central events before decreasing in peripheral events. This effect can be directly linked to the formation of the Quark-Gluon Plasma (QGP) in the early stages of the collision, where the production of heavy quarks also occurs.

This behavior is primarily attributed to two distinct effects. The rapid motion of the charged nuclei generates a considerable magnetic field oriented perpendicular to the event plane. Heavy quarks, possessing a magnetic moment, are expected to be polarized as they traverse this magnetic field.

Another physical effect that modulates the polarization is the vorticity of the medium. The QGP formed in heavy-ion collisions is believed to possess the largest vorticity ever observed in the universe. This large vorticity generates an orbital angular momentum within the medium, whose direction is typically aligned perpendicular to the reaction plane (and therefore, related to the event plane). This phenomenon causes the polarization of quarkonia states, such as the J/ψ, through spin-orbit coupling.

Chapter 4

Concluding Remarks

4.1 Summary

The analyzed data provides strong evidence of J/ψ polarization within the studied pT ranges, supported by the significant results obtained from the hypothesis testing. The observed dependence of collision centrality highlights the critical role of the medium's properties in affecting J/ψ polarization, attributed to the formation of Quark Gluon Plasma (QGP) in the early stage of the collision, affecting the heavy quarks produced in the same instance due to the magnetic field and orbital angular momentum in the direction perpendicular to the eventplane. Furthermore, our results show consistency with the measurements reported by the ALICE Collaboration, despite focusing on a higher pT range.

What differentiates our study from ALICE's is the fact that we have used an angular distribution generated with Pythia events, in such a way that it is unpolarized, to compare both distributions. In contrast, they use a random rotation per event to the axis perpendicular to the event plane to calculate $\cos(\theta)$, obtaining a flat distribution.

We believe that a more robust result would be to use ATLAS Monte Carlo simulations where prompt J/ψ are generated and their detection is also simulated.

4.2 Future directions

Our proposed future work involves implementing several distinct data correction methodologies. Applying a correction for detector acceptance is crucial, as it is

expected to significantly enhance the quality of the measured distribution. While the resulting λ_θ values and the outcome of the hypothesis test may exhibit variations, we anticipate a persistent and strong indication of polarization, particularly within the lowest pT range studied.

A similar refinement is necessary for the event plane determination. Although the current data processing successfully establishes the correct perpendicular direction, improving this calculation will positively impact the overall precision of the measurements.

As a final, logical step, we must generate Monte Carlo (MC) events to simulate the production and detection of an unpolarized distribution. This simulated data will be directly incorporated into the hypothesis test.

REFERENCES

[1] E. Eichten, K. Gottfried, T. Kinoshita, K. D. Lane, and T.-M. Yan, "Charmonium: The model," *PHYSICAL REVIEW D*, vol. 17, no. 11, pp. 3090–3117, JUNE 1978.

[2] C. L. Pietro Faccioli, *Particle Polarization in High Energy Physics, An Introduction and Case Studies on Vector Particle Production at the LHC*, 1st ed. Tiergartenstrasse 17 69121 Heidelberg, Germany: Springer, 2023.

[3] P. Faccioli, "Towards the experimental clarification of quarkonium polarization," *Euro. Phys. J. C*, Jun. 2010.

[4] S. (Particle Data Group), "Review of particle physics."

[5] ALICE Collaboration, "Measurement of the j/ψ polarization with respect to the event plane in pb-pb collisions at the lhc," *Phys. Rev. Lett.*, vol. 131, no. 042303, 2023.

[6] ATLAS Collaboration, "Muon reconstruction performance of the atlas detector in proton-proton collision data at $\sqrt{s} = 13$ tev," *Eur. Phys. J. C*, vol. 76, no. 292, 2016.

[7] ——, "Muon reconstruction and identification efficiency in atlas using the full run 2 pp collision data set at $\sqrt{s} = 13$ tev," *Eur. Phys. J. C*, vol. 81, no. 578, 2021.

[8] D. Griffiths, *Introduction to elementary particles.*, 1st ed. United States: OHN WILEY SONS, INC., 1987.

[9] KAUST, *Thesis and Dissertation Guidelines*, 1st ed. Thuwal, Makkah Province, Saudi Arabia: KAUST, 2011.

[10] A. Sharma, M. M. Aggarwal, and A. K. Bhati, "Event plane determination," in *ALICE-INDIA COLLABORATION MEETING*, VECC, Kolkata, mar 2017.

[11] E. Lelák, "Study of jet suppression in heavy-ion collisions with the atlas experiment," Ph.D. dissertation, Institute of Particle and Nuclear Physics, 2024.

[12] R. Novotný, "J/ polarization studies using the atlas detector," Ph.D. dissertation, Czech Technical University in Prague Faculty of Nuclear Sciences and Physical Engineering, 2016.

[13] M. Thomson, *Modern Particle Physics*, 1st ed. University Printing House, Cambridge CB2 8BS, United Kingdom: Cambridge University Press, 2013.

[14] A. Collaboration, "The atlas experiment at the cern large hadron collider: A description of the detector configuration for run 3," *Journal of Instrumentation (JINST)*, vol. 19, no. 05, p. P05063, Jun. 2024.

[15] S. Narison, *QCD as the Theory of Hadrons: From Partons to Confinement*, 2nd ed. United Kingdom: Cambridge University Press, 2023.

[16] L. McLerran, "Relativistic heavy-ion physics: three lectures," *Lectures on Quark Matter*, vol. 583, no. NULL, pp. 75–114, NULL 2002.

[17] ATLAS Collaboration, "Heavy ion trigger public results," http://twiki.cern.ch/twiki/bin/view/AtlasPublic/HeavyIonTriggerPublicResults, CERN, ATLAS Experiment, 2024.

[18] ——, "Heavy ion physics documentation," https://opendata.atlas.cern/docs/documentation/introduction/heavy_ions, CERN, ATLAS Open Data Project, 2024.

[19] ——, "Atlas experiment schematics and diagram resources," https://atlas.cern/Resources/Schematics, CERN, ATLAS Experiment, 2024.